Developing controllable anisotropic wet etching to achieve silicon nanorods, nanopencils and nanocones for efficient photon trapping

Ho-Yuen Cheung,[‡] Hao Lin,[†] Fei Xiu,[†] Fengyun Wang,[†] TakFu Hung,[†] Johnny C. Ho[†,*], Chun-Yuen Wong[‡,*]

[†] Department of Physics and Materials Science, City University of Hong Kong, Tat Chee Avenue, Kowloon Tong, Kowloon, Hong Kong

[‡] Department of Biology and Chemistry, City University of Hong Kong, Tat Chee Avenue, Kowloon Tong, Kowloon, Hong Kong

TEL&FAX: 3442 4897 / 3442 0538

[*E]-mail: johnnyho@cityu.edu.hk

Abstract

This paper introduces a simple wet-chemistry based anisotropic etching for fabricating high aspect ratio nano-arrays with different morphologies. This method has a great potential for application of producing efficient, low-cost and large-scale photon trapping devices.

1. Introduction

Since silicon (Si) nanostructures, including nanowires, nanopillars and nanocones, contain unique optical and electrical properties and extraordinary surface-area-to-volume ratio, they have been widely used in device applications such as solar cell sensors, vertical transistors, etc. in recent years. One of the famous methods for fabricating those nanostructures with high aspect ratio is reactive ion etching (RIE). Yet, the drawbacks include high cost, induced damage of the crystal orientation on the surface and chemical contamination. On the other hand, using wet anisotropic etching approach to produce sharp and well-controlled features has not been well achieved because of the difficulties in choosing appropriate chemicals as etchants. Most of the etchants preferentially erode the underlying substrate in an isotropic manner. Here, we introduce a simple wet-chemistry-only fabrication scheme for the controllable hierarchy of highly regular, single-crystalline and high aspect ratio Si nanostructures with different geometrical morphologies, ranging from nanorod, nanopencil and nanocone arrays. Moreover, these nano-arrays can be manipulated with tunable dimensions and spacing over a wide range in large areas, which is particularly attractive for applications requiring efficient photon trapping (e.g. photovoltaics).

2. General Experimental Details

In this work, the Si nanopilliar array acted as fabrication templates made by nano-sphere lithography using polystyrene (PS) nanospheres followed by the metal-assisted chemical etching. Briefly, the Ti/Au mesh film is deposited on the Si surface, then is performed etching in HF/H_2O_2 solution. The fabricated templates were next treated with a mixture of $AgNO_3$, HF, and HNO_3 or H_2O_2 for the selective deposition of Ag clusters on the nanopillar tips for the further Si etching. Figure 1 shows the SEM images of different morphologies of nanopillar arrays manipulated by a number of repeating times of Ag cluster deposition and removal processes.

3. Results and Discussion

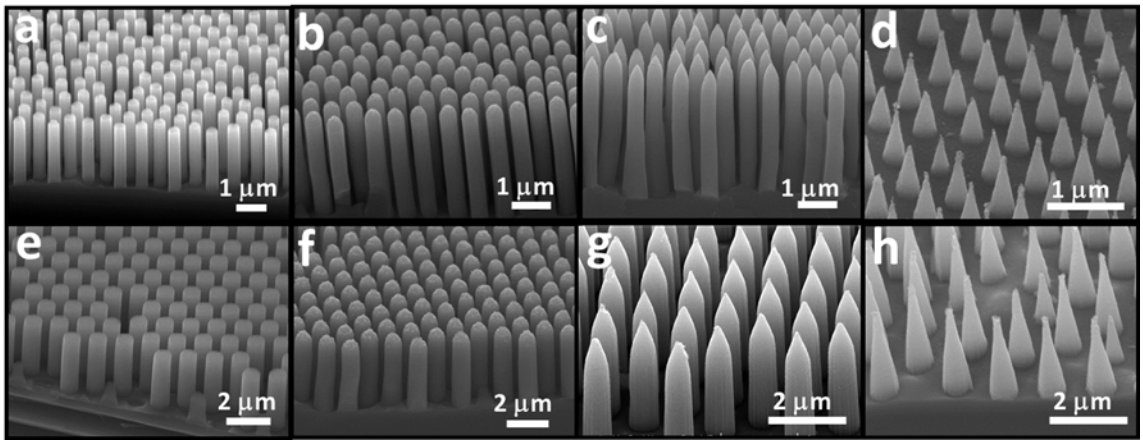

Fig. 1. Representative SEM images of nano-arrays with different geometrical morphologies (ranging from nanopillars, nanorods, nanopencils to nanocones; panel a to d with the pitch of 0.7 μm; panel e to h with the pitch of 1.3 μm). © Royal Society of Chemistry

Figure 2 shows the proposed formation mechanism of different morphologies of such arrays. The fabrication templates were first etched by [$AgNO_3$+ HF + HNO_3 / H_2O_2] system. The anisotropic behavior was due to the presence of Ag clusters which acted as catalysts formed by $AgNO_3$. Because of the difference of crystallinity, the Ag clusters

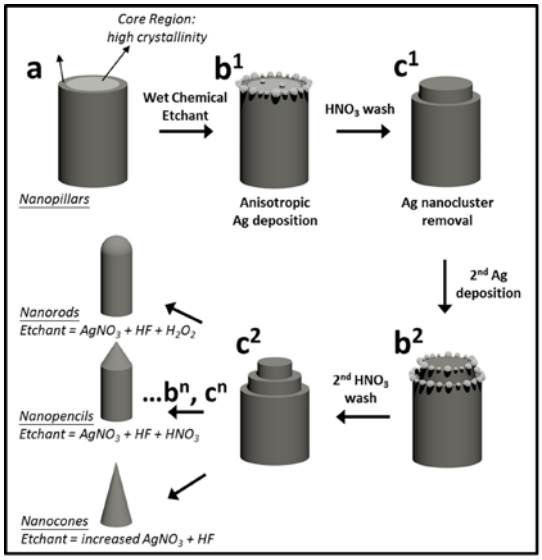

Fig. 2 Schematic illustrations of the formation mechanism of Si nanostructures with different morphologies observed in Fig. 1. © Royal Society of Chemistry

were mainly formed at the apical position of each nanopillar. The morphological difference could be controlled by the concentration of $AgNO_3$ (nanocone formed from higher concentration) and changing the oxidant (nanorod formed by using H_2O_2 instead of HNO_3)

Figure 3 shows the UV-vis reflectance measurement in the spectral range of 400 – 800 nm of Si nanopillars with different morphological geometries. According to the reflective spectra, nanorods and nanopencils exhibit very low reflectance down to <5% compared to the nanopillar

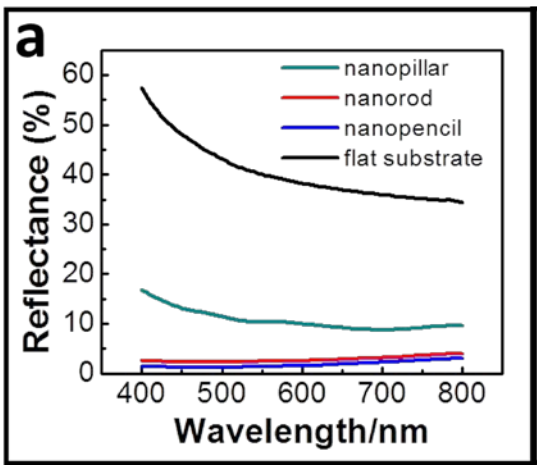

Fig. 3 Optical reflectance measurement of different fabricated morphological nanopillar arrays. Nanopillars, nanorods and nanopencils with the pitch of 0.7 μm and 2 μm depth. © Royal Society of Chemistry

and bare flat substrates, which is mainly due to the apical region with a smaller pillar diameter for more efficient photon capturing, trapping and transmission down to the base region with a higher material filling ratio and enhanced absorption.

4. Conclusion

Si nanorod, nanopencil and nanocone arrays with large scale have been successfully fabricated by the simple wet-chemistry. Those fabricated nano-arrays were shown with high performance for photon trapping ability.

Reference

[1] H. Lin, H. Cheung, F. Xiu, F. Wang, S. Yip, N. Han, T. Hung, J. Zhou, J. C. Ho and C. Wong, *J. Mater. Chem. A*, 2013, **1**, 9942

Iron Phthalocyanine Coated Carbon Nanohorn for Oxygen Reduction Reaction in Proton Exchange Membrane Fuel Cells (PEMFCs)

Guofa DONG, Fengyun WANG, Johnny C. HO*

Department of Physics and Materials Science, City University of Hong Kong, 83 Tat Chee Avenue, Kowloon, Hong Kong
TEL&FAX: +852-3442 4897，+852-3442 0538
*E-mail: johnnyho@cityu.edu.hk

Abstract

A composite of iron phthalocyanine (FePc) coated carbon nanohorn (CNH) was fabricated by a simple method and its catalysis on oxygen reduction reaction (ORR) was studied. Comparing with FePc, FePc/CNH composite shows much better catalytic property for ORR. The composite can give an ORR peak potential of -0.13 V, higher than the potential on commercial Pt/C. The composite also has a good selectivity for ORR when methanol coexists.

1. Introduction

Oxygen reduction reaction (ORR) is a fundamental process for the energy transfer in PEMFCs. The reactive efficiency of ORR will determine the entire performance of a PEMFCs[1]. Up to now, the most efficient ORR catalysts in commercial application are still platinum (Pt) or Pt-based materials, but Pt is a noble metal and its reservation is limited[2]. So developing cheap and high-performance ORR catalysts is a main task in the research of PEMFCs.

Metallic phthalocyanines (MPc, shown in Fig. 1) are macrocycle molecules and used as dyes for many years. MPcs are also perfect catalysts for many electrochemical reactions[3]. In 1964, Jasinski first reported that CoPc held

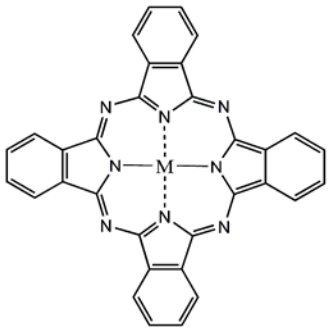

Fig. 1 Scheme of metallic phthalocyanine

good catalytic property on ORR in alkaline media[4]. From then on, many different catalysts based on MPcs for ORR are developed[5, 6], but being prone to aggregation[7, 8] and its poor electric conductivity[9] limit the electrocatalytic performance of MPc. To improve the performance of MPc, many carbon nanomaterials such as carbon nanotubes, carbon fibers and graphene, have been used for loading MPcs to improve the dispersion of MPc and accelerate the electron transfer[10, 11]. The ORR catalytic performance of the composite based on MPc was enhanced a lot, but it still needs a further improvement to meet the common applications.

Carbon nanohorn (CNH) is an individual particle composed of an aggregate of many horn-shaped sheaths of graphene sheets[12]. Its shape looks like dahlia or bud, and it holds very large surface area, excellent electrical conductivity and outstanding thermal and chemical stability. It is an ideal supporter[13, 14]. Here we select carbon nanohorn as the supporter and fabricate a composite of FePc and CNH by a simple method in order to improve the catalytic performance of FePc on ORR and achieve a close to perfect ORR catalyst.

2. Experimental section

2.1 Preparation of the Composite

Iron Phthalocyanine (FePc) was commercially available. Carbon nanohorn was produced by a direct current arc discharge[15]. The composite of FePc and CNH was fabricated by mixing of FePc and CNH in $CHCl_3$ under ultrasonication for 8 hours, then the black suspension was stirred and kept still for 10 hours. The final composite was separated from the solution by vacuum rotary evaporation and then dried under vacuum and 80 ^oC overnight. The

commercial Pt/C (20 wt % Pt on Vulcan XC-72) was obtained from Alfa Aesar.

2.2 Characterization

The final composite was denoted as FePc/CNH and characterized by Fourier Transform infrared (FTIR) spectroscopy, and transmission electron microscopy (TEM, Philips CM-20).

2.3 Electrochemical Measurements

Electrochemical measurements were performed on an electrochemical workstation (CHI 660C). A standard three-electrode electrochemical system connected with a gas flow systems was employed. A glassy carbon disk electrode (GCE, diameter of 5 mm), an Ag/AgCl (saturated KCl-filled) electrode and a platinum wire were used as the working electrode, reference electrode and counter electrode, respectively. The ORR performance of the catalysts was determined by cyclic voltammogram (CV) measurements in an aqueous solution of 0.1 M NaOH. CV curves were recorded at a scan rate of 100 mV s^{-1}.

The electrode surface was polished with the slurry of α-Al_2O_3 powder with different particle sizes (500nm, 100nm, and 50 nm), then washed with DI water, ethanol, and DI water accordingly and separately for 5 minutes and finally dried in hot air. For modifying the GCE, 2.0 mg FePc/SWCNT, 1.0 mL isopropanol and 50.0 μL Nafion (Du Pont Corp., 5 wt %) were mixed into a ink. 30 μL of the ink was loaded on the GCE surface. For comparison, the GC electrodes coated with FePc, SWCNT or Pt/C (20 wt % Pt on Vulcan XC-72) were also fabricated with the same procedure.

3. Results and Discussion

3.1 Characterizations of FePc/CNH

Fourier Transform infrared (FTIR) spectroscopy is a common and powerful tool to characterize materials, and it can provide the characteristic peaks for one certain compound. The FTIR spectra of CNH, FePc and FePc/CNH are shown in Fig. 2. FePc shows rich and strong characteristic peaks but there are just a few weak characteristic peaks for CNH. In the FePc/CNH composite the characteristic peaks from FePc are very

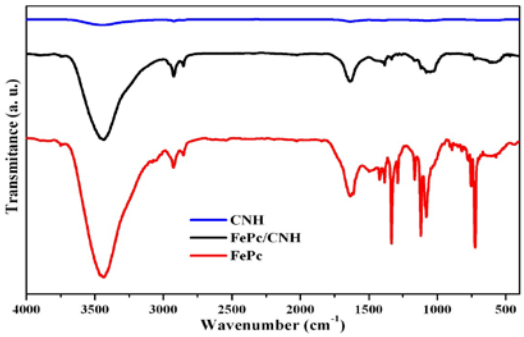

Fig. 2 Infrared spectra of CNH, FePc and FePc/CNH

obvious, but the intensities of these peaks become weak, which may be attributed to the π-π electronic interaction between FePc and the graphene layer of CNH. From the FTIR spectra, it can be concluded that FePc was loaded on the CNH successfully. The TEM images of CNH and FePc/CNH are shown in Fig. 3. The CNH is very neat and its layers can be observed clearly in Fig. 3(a), but after

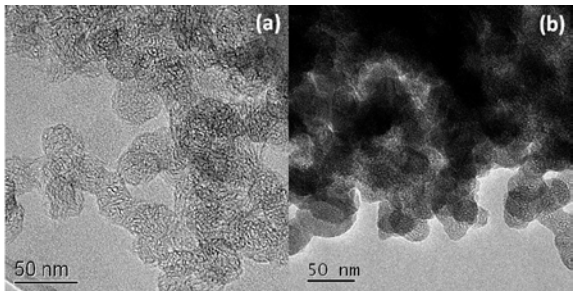

Fig. 3 TEM images of CNH (a) and FePc/CNH composite (b)

mixing with FePc the structure of CNH becomes vague due to the black material covered on the surface. Obviously it is the layer of FePc fixed on CNH.

3.2 Electrochemical Performance of the FePc/CNH for ORR Catalysis

ORR activity was determined based on steady-state polarization curves, which were recorded after 20 pre-sweeps. Fig. 4 shows the CV curves of FePc/CNH in NaOH solution saturated by N_2 and O_2, respectively. In N_2 saturated solution, only some weak

peaks can be found and these peaks may result from the intrinsic properties of FePc/CNH. In O_2 saturated solution, a strong peak is achieved at a potential of -0.13 V, which is obviously caused by the ORR.

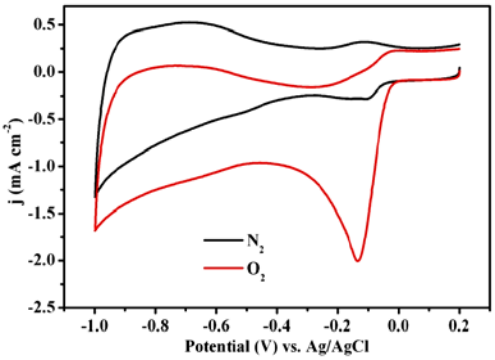

Fig. 4 CVs of FePc/CNH in 0.1 M NaOH solution saturated with N_2 (black) or O_2 (red)

The CV curves for FePc and CNH in O_2 saturated NaOH solution are shown in Fig. 5 for comparing the ORR activity of different materials. It can be found that the peak potential on FePc/CNH composite is the highest of the three and it is 40 mV and 240 mV higher than FePc and CNH, respectively. The peak current intensity on FePc/CNH composite is also the highest of the three values, and it increases to -2.01 mA cm^{-2} which is about twice of the peak current catalysis, comparing with FePc. This can be attributed to the high dispersion of FePc and fast electron transfer by CNH. The catalytic activity of the FePc/CNH composite for ORR is also compared with the commercial Pt/C, which is shown in Fig. 6. There is an increase about 40 mV in potential for FePc/CNH comparing with Pt/C.

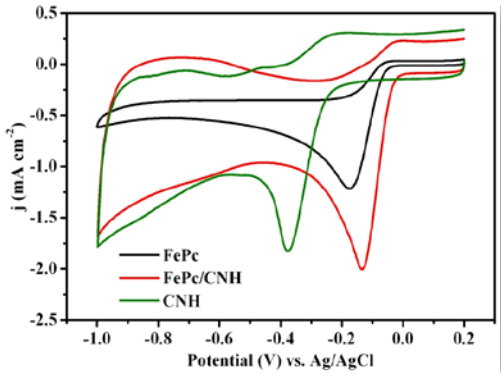

Fig. 5 CVs of FePc, CNH and FePc/CNH in 0.1 M NaOH solution saturated with O_2

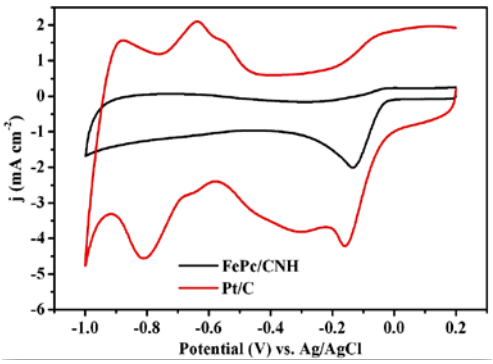

Fig. 6 CVs for Pt/C and FePc/CNH in 0.1 M NaOH solution

The selectivity for ORR is also an important property for an efficient ORR catalyst. Though Pt-based catalysts have high activity for ORR, they often suffer from a crossover effect caused by the interference of carbon oxide, methanol and so on, and then lose their ORR catalytic activity completely. Here, the ORR selectivity of FePc/CNH composites was also assessed and shown in Fig. 7. For FePc/CNH there is almost no

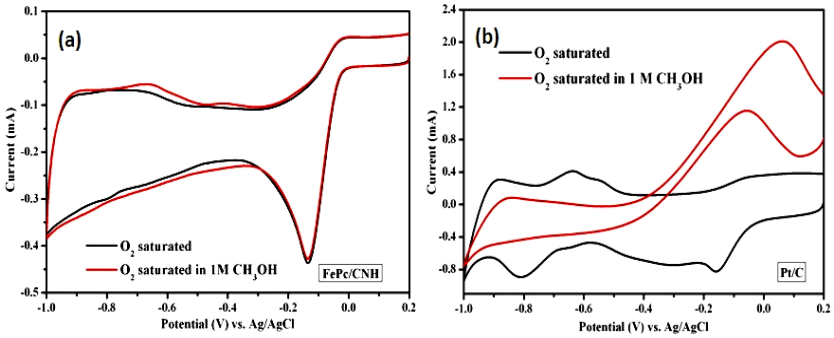

Fig. 7 CVs of FePc/CNH (a) and Pt/C (b) in 0.1 M NaOH solution saturated with O_2 with and without 1 M CH_3OH.

apparent change before and after 1 M CH_3OH was added into the NaOH solution (Fig. 7 (a)), which implies that FePc/CNH composite has a high selectivity for ORR. But there is an obvious change in the CV curves of Pt/C and the ORR peak at -0.17V disappeared completely and two new upside peaks at -0.06 V and 0.07 V appear after the addition of CH_3OH.

4. Conclusion

In conclusion, we have prepared a composite of FePc and CNH, and also studied its catalytic performance for ORR. The FTIR spectra and TEM images proved that FePc was fixed on CNH successfully. The electrochemical results implied that FePc/CNH shows good activity and selectivity for ORR and it is an excellent catalyst for the reduction of oxygen.

Reference

1. A. Morozan, S. Campidelli, A. Filoramo, B. Jousselme and S. Palacin, *Carbon*, 2011, **49**, 4839-4847.
2. F. Jaouen, E. Proietti, M. Lefevre, R. Chenitz, J. P. Dodelet, G. Wu, H. T. Chung, C. M. Johnston and P. Zelenay, *Energ Environ Sci*, 2011, **4**, 114-130.
3. J. H. Zagal, *Coordin Chem Rev*, 1992, **119**, 89-136.
4. R. Jasinski, *Nature*, 1964, **201**, 1212-1213.
5. L. Ding, Q. Xin, X. J. Zhou, J. L. Qiao, H. Li and H. J. Wang, *Journal of Applied Electrochemistry*, 2013, **43**, 43-51.
6. L. N. Ramavathu, K. K. Maniam, K. Gopalram and R. Chetty, *J Appl Electrochem*, 2012, **42**, 945-951.
7. P. Prochnow, M. Wark, G. Schulz-Ekloff, D. Wohrle, A. Zukal and J. Rathousky, *J Porphyr Phthalocya*, 2002, **6**, 494-501.
8. L. C. Gruen, *Aust J Chem*, 1972, **25**, 1661-&.
9. Y. Harima and K. Yamashita, *J Appl Phys*, 1991, **69**, 7081-7086.
10. G. F. Dong, M. H. Huang and L. H. Guan, *Physical Chemistry Chemical Physics*, 2012, **14**, 2557-2559.
11. Y. Yuan, B. Zhao, Y. Jeon, S. K. Zhong, S. G. Zhou and S. Kim, *Bioresource Technology*, 2011, **102**, 5849-5854.
12. S. Iijima, M. Yudasaka, R. Yamada, S. Bandow, K. Suenaga, F. Kokai and K. Takahashi, *Chem Phys Lett*, 1999, **309**, 165-170.
13. G. Mountrichas, S. Pispas, T. Ichihasi, M. Yudasaka, S. Iijima and N. Tagmatarchis, *Chem-Eur J*, 2010, **16**, 5927-5933.
14. K. Ajima, T. Murakami, Y. Mizoguchi, K. Tsuchida, T. Ichihashi, S. Iijima and M. Yudasaka, *Acs Nano*, 2008, **2**, 2057-2064.
15. N. Li, Z. Y. Wang, K. K. Zhao, Z. J. Shi, Z. N. Gu and S. K. Xu, *Carbon*, 2010, **48**, 1580-1585.

Monolayer molecular doping for cost-effective Si photovoltaics

Fei Xiu, Johnny Ho*

Department of Physics and Materials Science, City University of Hong Kong, 83 Tat Chee Ave., Kowloon Tong, Kowloon, Hong Kong
*E-mail: johnnyho@cityu.edu.hk

Abstract

This paper introduces our recently developed low-cost, scalable, monolayer surface doping of semiconductor materials for the Si photovoltaic device fabrication without using conventional costly doping schemes such as the ion-implantation. This novel technique is based on the formation of self-assembled monolayers of dopant-containing molecules on the surface of Si followed by the subsequent thermal diffusion of dopant atoms via rapid thermal annealing. To maximize the absorbed light into the device, surface of crystalline silicon wafer is randomly texturized by the chemical anisotropic etching. In our preliminary study, energy conversion efficiency of ~6% under the illumination of AM1.5G is achieved based on this process scheme.

1. Introduction

In the past decades, diminishing supplies in natural fuel resources and environmental issues from combustion gases highlight the need for new energy sources [1–3]. Being clean, renewable and universally abundant, solar energy is a viable choice to meet the increasing energy demand. However, it is also the least harvested form of renewable energy.[2] The major obstacles come from the substantial fabrication and materials costs of existing high performance silicon solar cells which are not economical for terrestrial daily applications, due to the fact that solar cell modules already take up approximately 60 % of the total cost for the solar power installation.[3] In this regard, tremendous effort has been made to develop highly efficient and low-cost Si photovoltaic devices.

Typical solar cells rely on p/n junctions to collect the photo-generated electron-hole pairs and then convert them into electricity.[4] During fabrication processes, impurities such as dopants are thermally introduced to the Si crystal to produce those junctions; however, this is not possible to control the junction profile near the surface region to attain so-called shallow junctions (USJs) to push the ultimate energy conversion to the thermodynamic efficiency limit.[4] Device physics modeling has shown that the formation of ultra-shallow junction is preferred to achieve high PV efficiency since the majority part of electron-hole pair optical generation occurs just below the surface of the devices. Thus the shallow junction can effectively separate charge carriers.

Recently, we have developed an innovative approach to achieve the low-cost, large-scale, high throughput and controllable monolayer doping (MLD) for shallow junctions in Si, which is based on the formation of self-assembled monolayers of dopant-containing molecules on the Si surface followed by the subsequent thermal diffusion of dopant atoms via rapid thermal annealing.[5,6] Notably, in contrast to the competing technologies, monolayer doping does not require expensive vacuum equipment and long vacuum process time which is attractive to be used as a mass-production platform. By texturizing the substrate into randomly distributed pyramid structure, light absorption properties of the device is improved which contributes to the higher conversion efficiency. In our initial study, energy conversion efficiency of 6.2 % under the illumination of AM1.5G was achieved based on this process scheme.

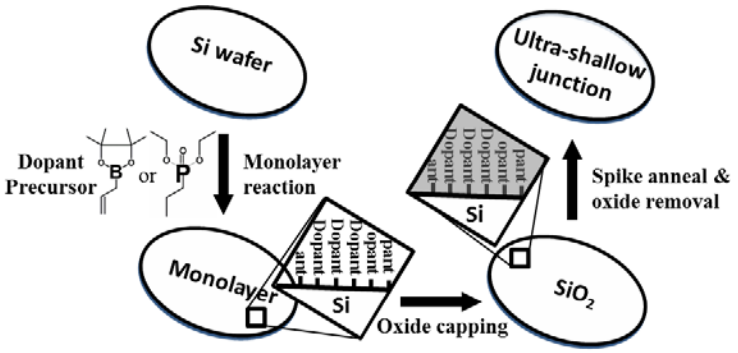

Figure 1 Schematic of the shallow junction formation process.

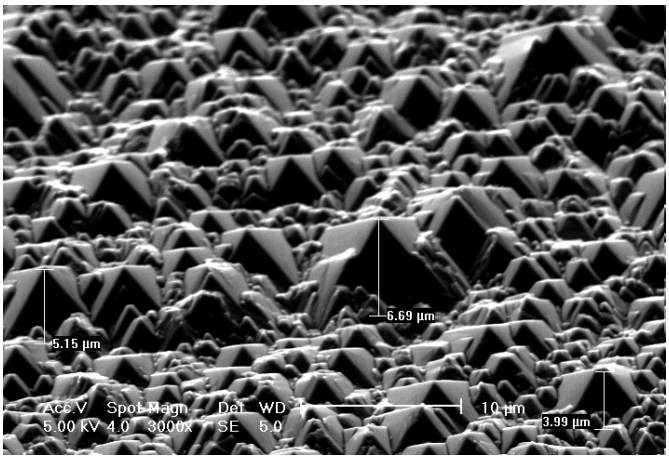

Figure 2. SEM images of the Si pyramid structure.

2. n^+/p junction formation by MLD and photovoltaic device fabrication

For the phosphorus-MLD (P-MLD) process, p-type Si wafers were first treated with dilute hydrofluoric acid to remove the native SiO_2 in the glove box. The Si surface was then reacted with diethyl 1-propylphosphonate (DPP, Alfa Aesar) and mesitylene as a solvent (25:1, v/v) for 2.5 h at 120 °C to assemble a P-containing monolayer [6, 7]. Following, a layer of 50 nm thick SiO_2 is electron-beam evaporated as a cap, and the substrate is spike annealed between 900-1050 °C in Ar ambient to drive in the P atoms and achieve n+/p USJs. The spike annealing is performed in a rapid thermal processing tool with a fast ramping rate of 100°C/s to the target temperature. Schematic of shallow junction formation process is demonstrated in Figure 1.

After the formation of n+/p junction, ITO and Ni were deposited as the top and bottom electrodes, respectively. Ag finger grids were then thermal evaporated on top of the ITO layer to help collecting charge carriers more effectively.

3. Results and Discussion

Here the random Si pyramid structure was achieved by the chemical anisotropic etching using a potassium hydroxide and isopropyl alcohol solution under 80 °C. It could be observed from Figure 2 that the Si substrate has been well texturized with random pyramids with an average height of ~ 8 um.

Light reflection of the planar silicon wafer and silicon pyramid structures etched for different etching time is compared in Figure 3. It is found that light reflection of

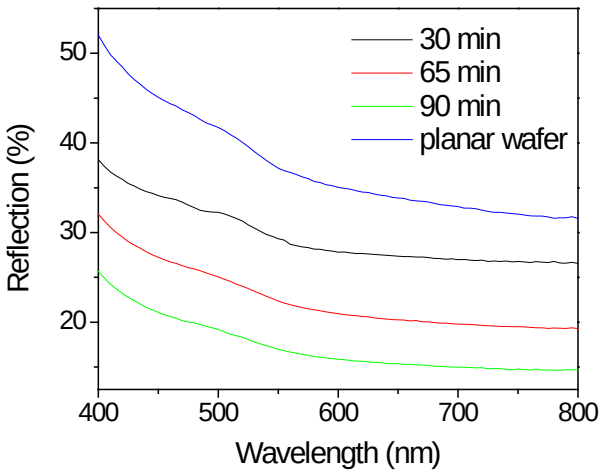

Figure 3. Light reflection property of Si wafer and Si pyramid structures.

pyramid structures is much lower than the untreated Si wafer, indicating a better light absorption property of the pyramid structure. Notably, as the etching time increases, light reflection of the obtained pyramid structure decreases. And the pyramid structure under 90 min etching shows the lowest light reflection property.

On the other hand, to decrease the back contact side carrier recombination, a rear p+ back surface doping is achieved by ion implantation with boron. Sheet resistance of the back side of the wafer is measured by the four point probing and a low sheet resistance of 24 ohm/sq is achieved. Solar cell devices are then fabricated after the deposition of contacts, as shown in Figure 4, and corresponding photovoltaic performance is investigated by solar simulation under AM 1.5G.

Figure 5 demonstrates the I-V characteristics of pyramid structured solar cell device with p+ back side doping. This pyramid solar cell has the Voc of 0.45 V, Jsc of 28.6 mA/cm^2 and fill factor (FF) of 48.34%, with the energy conversion efficiency of 6.2 % under AM1.5G illumination.

For the qualitative comparison, Table 1 summarized the Voc, Jsc, FF and efficiency values of the solar cell devices with different surface structures and the effect of p+ back

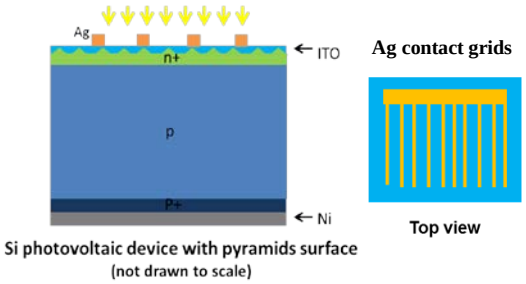

Figure 4. Schematic of the pyramid solar cell device structure with the p+ back side doping.

side doping. Contrasted with the planar device, there is a great improvement in Jsc and conversion efficiency for the pyramid solar cells due to the efficient light trapping properties of the pyramid structure. A little decrease in FF after the pyramid texturizing is observed probably because of the increase in the series resistance. After the formation of p+ layer in the back side by the boron doping, Jsc is improved significantly for both planar and pyramid devices. The p+ doping formed at the back side of Si substrate could generate an inner electric field to repel photo-induced minority carriers at the backside and decrease the back-surface recombination, which leads to the improvement of Jsc.

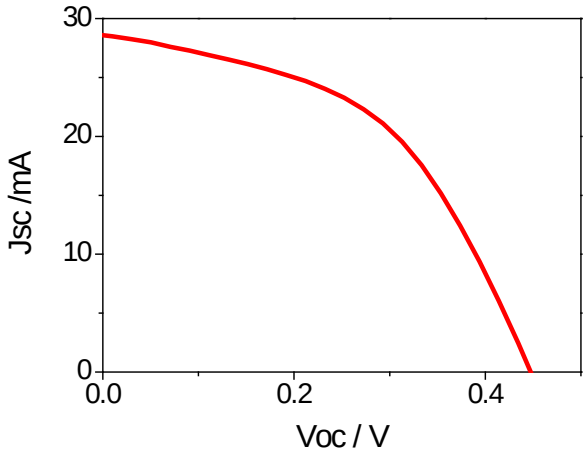

Figure 5. I-V characteristics of the pyramid solar cell device with p+ back side doping.

Table 1. Performance parameter of solar cell devices with different structures.

Device structure	**Voc (V)**	**Jsc (mA/cm^2)**	**Fill Factor (%)**	**Efficiency (%)**
$n^+/p/p^+$ (planar)	0.44	21.49	53.97	4.99
n^+/p (planar)	0.46	15.31	64.76	4.52
$n^+/p/p^+$ (pyramids)	0.45	28.61	48.34	6.2
n^+/p (pyramids)	0.41	23.8	52	5.03

4. Conclusion

In this work, studies of monolayer doping approach for the shallow p-n junction formation and application in single crystalline silicon solar cells were presented. This cell fabrication process is a simple and low-cost approach based on a phosphorus doping step achieved by the monolayer doping technique at the front to create the n+/p junction. In our study, 6.2% efficiency was accomplished based on the pyramid surface texturization. To further explore the higher photovoltaic performance, additional studies on the fabrication of three-dimension (3D) nanostructured solar cell devices with superior light harvesting properties will be carried out.

Reference

[1] M. S. Dresselhaus, I. L. Thomas, Nature. 414(2001) 332–337.
[2] M. Grätzel, Nature. 414(2001) 338–344.
[3] G. Goncher, R. Solanki, Proc. SPIE.

(2008) 7047.
[4] A.L. Fahrenbruch, R.H. Bube, Fundamentals of Solar Cells: Photovoltaic Solar Energy Conversion, New York: Academic Press, Inc. (1983).
[5] J.C. Ho, R. Yerushalmi, Z.A. Jacobson, et al., Nat. Mater. 7(2008) 62-67.
[6] J.C. Ho, R. Yerushalmi, G. Smith, P. Majhi, et al., Nano Lett. 9(2009) 725-730.

Surface roughness induced electron mobility degradation in InAs Nanowire

SenPo Yip, Fengyun Wang, Ning Han, KitWa Fok, Guofa Dong, TakFu Hung, K S Chan, Johnny C Ho*

Department of Physics and Materials Science, City University of Hong Kong, 83 Tat Chee Avenue, Kowloon Tong, Kowloon, Hong Kong
TEL: +852-3442-4897
*E-mail: johnnyho@cityu.edu.hk

Abstract

In this work, the surface roughness dependent electron mobility in InAs nanowires is studied. The electron mobility of InAs nanowires degrades monotonically as the nanowire surface roughness increases after detailed electrical characterizations. Under low temperature measurements, the surface roughness shows a dominant impact on the electron mobility after the surface/interface traps and phonon scattering have been decoupled. All these highlight that the nanowire geometries and surface conditions must be carefully considered for the device design of optimal performances.

1. Introduction

III-V semiconductor nanowires (NWs), especially InAs NWs with the high electron mobility, have attracted large research interests as channel materials for high-performance transistors. The electrical properties of these NWs are dependent on their dimension and surface condition due to its high surface-to-volume ratio. This work presents a semi-quantitative study of the dependency of electron mobility on the surface roughness of InAs NWs, in which the intrinsic electron mobility decreases with the increase of surface roughness. The dominant role of the surface roughness scattering on the electron mobility degradation is highlighted under the low-temperature electrical device characterization. The experimental results are important for the design and optimization of device performance constructed by NWs.

2. Experimental

InAs NWs investigated here were obtained by a solid-source catalytic chemical vapor deposition (SSCVD). Briefly, 1.2 g of InAs powder (99.9999% purity) and Ni catalyst (0.2 nm thick on the SiO_2/Si substrate and pre-annealed for 10min at 800 ^oC) were heated at the upstream (690 ^oC) and downstream (470 ^oC) zone of a tube furnace, respectively, under H_2 environment (200 sccm) at ~1.0 Torr for 60 min. The grown substrate was cooled down under H_2 environment. The grown InAs NWs were harvested by sonication in anhydrous ethanol and then were drop-casted onto a heavily doped Si wafer (with 50 nm thermal grown oxide on top) for fabricating back-gated field-effect transistors (FETs). The electrode positions were defined by standard lithography process. Followed by the 5 s of HF (1%) treatment (to remove the native oxide on the NW), the substrate was put into vacuum chamber for Ni (50 nm) deposition and then lift-off. Electrical characterization was performed in a cryogenic probe station (Janis ST-500) with a semiconductor parameter analyzer (Agilent 4155C). Transmission electron microscope (TEM) analysis was performed in JEOL 2100F by drop-casting the harvested NWs onto a copper grid.

3. Results and Discussion

The obtained NWs from SSCVD are long, dense, without tapering and free from surface coating on the substrate (Fig. 1a). Such NWs are ideal for studying the corresponding electrical properties because any tapering and surface coating would degrade the mobility of NWs. The average diameter of these NWs is 31 ± 6 nm (Fig.

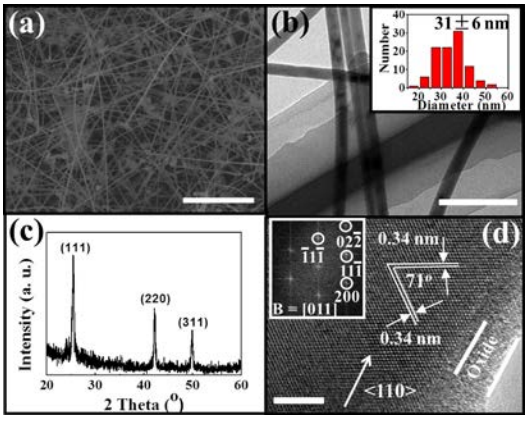

Figure 1. (a) SEM image of grown InAs NWs (scale bar = 2 μm). (b) TEM image of InAs NWs (scale bar = 200 nm). Insert is the diameter distribution of 100 NWs. (c) XRD spectrum of the grown InAs NWs. (d) HRTEM image of an InAs NW (scale bar = 5 nm). Insert is the relative FFT reciprocal lattice spots. [1] © 2013 IOP Publishing

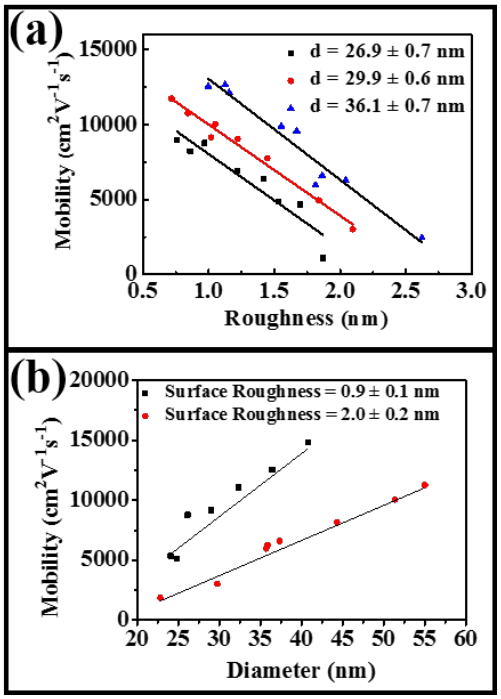

Figure 2. (a) Peak field-effect mobility as a function of surface roughness for NWs. (b) Peak field-effect mobility as a function of diameter for two different surface roughness ranges. [1] © 2013 IOP Publishing

1b), based on the TEM investigation of 100 NWs. All NWs obtained are zincblend in the crystal structure (Fig. 1c) and the dominant growth direction is <110>. A conformal native oxide layer (~3 nm) is observed which will be subtracted from the diameter for mobility calculation (Fig. 1d). After investigation of different NW devices with wide range of diameter and roughness, the mobility is observed to drop monotonically with increasing roughness with similar diameters (Fig. 2a); on the other hand, thick NWs have higher mobility than those of thin NWs when they have similar roughness. Furthermore, thinner NWs are more sensitive to the impact of surface roughness (Fig. 2b).

Low-temperature electrical measurements further emphasis the effect of surface roughness on mobility degradation by decoupling the effect of phonon scattering

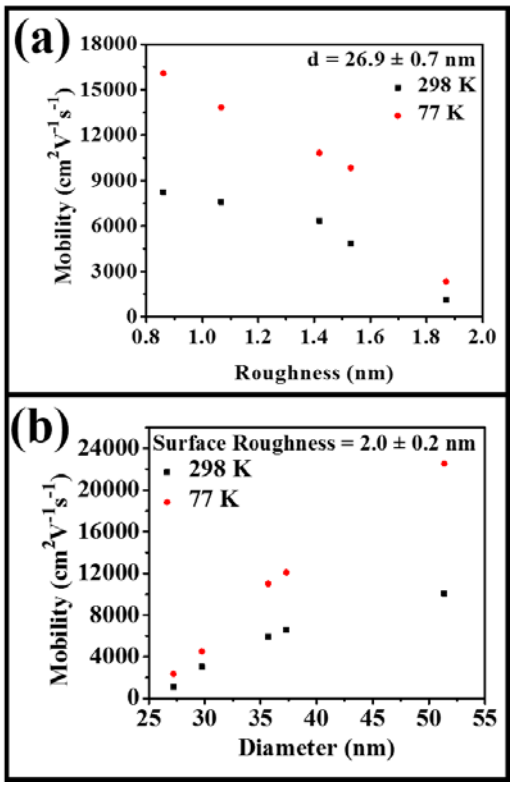

Figure 3. (a) Surface-dependent peak field-effect mobility of NWs with the diameter of 26.9 ± 0.7 nm measured at 77 K and 298 K. (b) NW diameter-dependent peak field-effect mobility of NWs with the surface roughness of 2.0 ± 0.2 nm measured at 77 K and 298 K. [1] © 2013 IOP Publishing

and thermal activated surface/interface traps. At 77 K, the mobility of all devices is improved. The improvement is more profound for smoother NWs. On the other hand, the field effect mobility has less improved at 77 K for thinner which highlights the dominant role of surface roughness scattering for thinner NWs because of the higher surface-to-volume ratio. All the experimental results highlight the impact of enhanced surface roughness to the field-effect mobility in miniaturized and surface disordered NWs.

Conclusion

In conclusion, this study presents a detail electrical characterization to investigate the effect of surface roughness on the mobility of InAs NW FETs. With the surface roughness increases, the mobility of the FET decreases monotonically. This effect is more profound with smaller diameter. Low temperature electrical characterizations further decouple the phonon scattering and surface/interface traps degradation and further highlight the dominant role of surface roughness induced degradation on mobility in both miniaturized and surface disordered NWs.

Reference

[1] Wang F.Y., Yip S. P. Han N. Fok K. W., Lin H., Hou J. J., Dong G., Hung T. F., Chan K. S., Ho J.C. "Surface roughness induced electron mobility degradation in InAs nanowire", *Nanotechnology*, **24**, 375202, 2013. doi:10.1088/0957-4484/24/37/375202

pH-responsive Graphene in Aqueous Suspensions

Ming Fang, Johnny C. Ho*

Department of Physics and Materials Science, City University of Hong Kong,
83 Tat Chee Avenue, Kowloon Tong, Kowloon, Hong Kong
TEL&FAX: +852-3442 4897/0538
*E-mail: johnnyho@cityu.edu.hk

Abstract

Homogeneous aqueous suspensions of graphene were prepared by chemical reduction of graphene oxide in the presence of chitosan. Strong noncovalent interactions between the graphene sheets and the chitosan molecular chains allow reversible manipulation of the sheets between well dispersed and more aggregated states by using pH-change as a stimulus. The strategy of using stimuli-responsive polymers to functionalize graphene opens up new opportunities for rational design of smart graphene based materials.

1. Introduction

Graphene has attracted huge attention recently due to its exceptional electronic, mechanical and thermal properties as well as great application prospects.[1–4] So far, graphene has been prepared by micromechanical cleavage,[5] chemical vapor deposition[6] and chemical reduction of graphene oxide (GO).[7] Unfortunately, as-produced graphene generally shows limited solubility in solvents, which hinders its practical applications in certain areas. This way, chemical modifications could serve as a powerful tool to solve this mentioned problem. Particularly, noncovalent modifications using dispersants/surfactants are often as used because they are not only simple for operation, but also cause no damage to the bonding structure of graphene. Various polymers and surfactants such as PSS,[8] PmPV,[9] and TWEEN[10] have been used to facilitate the dispersion of graphene in solutions. However, to our knowledge, little attention has been paid to the utilization of stimuli-responsive polymers as modifiers which could possibly endow graphene with more interesting properties.

Here, we demonstrate the use of chitosan, a pH-responsive biopolymer, as a noncovalent modifier to obtain homogeneous suspensions of graphene and show that the chitosan modified graphene sheets can be reversible manipulated between well-dispersed and aggregated states by applying pH-change as a stimulus.

2. Experimental

Graphite oxide was synthesized from graphite powder (<30μm) by a modified Hummers method.[11] A stock suspension of GO was obtained by sonication of the graphite oxide in water.[7] The GO suspension (100mL, 0.1mg/mL) was then gradually added to an acidic aqueous solution of chitosan (100mL, 0.5mg/mL, in 0.5 M HCl) with stirring to yield a uniform brown-colored dispersion. L-ascorbic acid powder (100 mg) was subsequently added to the above dispersion and the mixture was held at 60 °C for 6 h to reduce the GO into graphene.

3. Results and Discussion

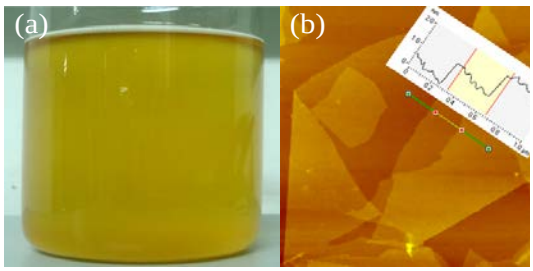

Fig. 1 (a) Aqueous suspension of exfoliated graphite oxide. (b) Typical AFM image of GO sheets deposited on a mica surface

Graphite oxide can be easily exfoliated and become monolayers in water under sonication. Obtained GO suspensions are brown colored and highly stable and AFM images show that the sheets are about 1.2 nm in thickness (Fig.1).

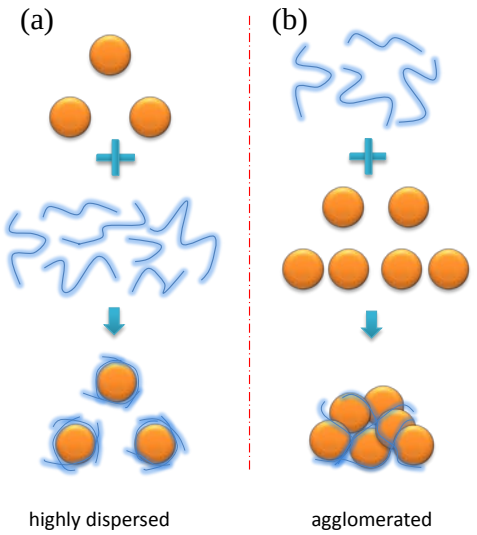

Fig. 2 Schematic illustration of the influence of the mixing manner on the properties of the mixtures. (a) Adding GO into a solution of chitosan produces a homogeneous dispersion. (b) Adding chitosan into a GO suspension leads to agglomeration of the GO sheets.

The GO suspensions were then used for preparations of GO/Chitosan solutions. Interestingly, we found that the mixing manner have huge influence on properties of the mixtures. Homogeneous GO/chitosan solution was prepared by simply adding a suspension of GO into a solution of chitosan under stirring. However, when we mix the two component solution in the opposite order, that is, adding a solution of chitosan into a suspension of GO, we get irreversible agglomerations. It is known that GO bears lots of carboxylic and hydroxyl groups and chitosan has abundant amino groups along its molecular chains. Ionizations of these functional groups in water make GO and chitosan charged, negatively for the former and positively for the latter, which was confirmed by ζ potential. While the GO suspension had a negative ζ potential of about -46 mV, the solution of chitosan held a positive ζ potential of about +100 mV. Once GO and chitosan meet with each other in solution, strong ionic interactions take place and yielded a new balanced system. The distinct dispersion states of GO sheets in different mixtures can be explained through the following model. As illustrated in Fig. 2, when GO was added to the solution of chitosan, chitosan is in mass relative to GO, and every GO sheet was immediately wrapped by large amounts of chitosan molecular chains through electrostatic attractions (ionic interactions), by which the GO sheets were isolated as individuals and a uniform dispersion formed. For mixing the two solutions in opposite order, there was a large excess of GO relative to the chitosan, and one chitosan polymer chain can possibly attached two or more GO sheets, leading to "bridging" flocculation.

Generally, GO can be chemically reduced into graphene. However, direct reduction of GO causes irreversible aggregations of the product, which is not favorable for its processing and applications. In this work, we used chitosan as the dispersant, and reduced

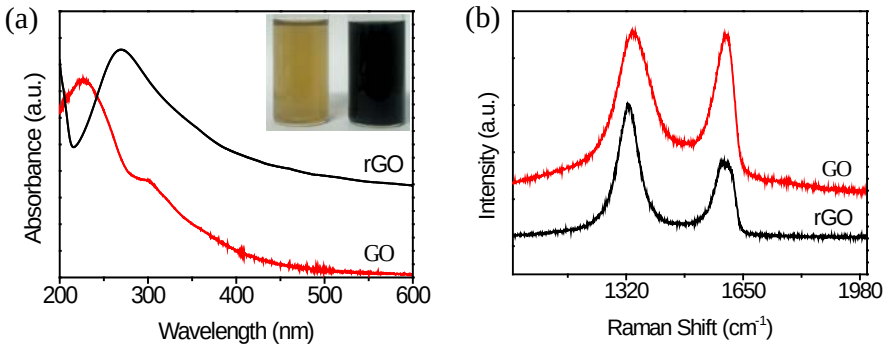

Fig. 3 (a) UV-vis absorption spectra of aqueous dispersions of bare GO and the reduced GO with chitosan. The inset shows the photographs of the dispersions. (b) Raman spectra of the GO and rGO.

the GO in situ by adding L-ascorbic acid (vitamin C) into a well-dispersed GO/chitosan suspension. After reduction, the suspension changed its color from light brown to dark, and no visible aggregation observed (Fig.3a, inset). The reduction was confirmed by UV-vis absorption spectroscopy and Raman spectroscopy. As shown in the UV-vis absorption spectra (Fig. 3a), after the reaction, the maximum absorption of the GO dispersion red-shifted from 230 to 270 nm, and meanwhile the absorption intensity in the entire spectrum (especially the region above 300 nm) dramatically increased, suggesting the restoration of the electronic conjugations in the sheets.[12] In the Raman spectra (Figure 3b), the reduced GO (rGO) gave a much higher intensity ratio of D band to G band (D/G, where the D band is induced by defects and the G band is due to the in-plane vibration of sp2 carbon atoms[13]). Since the Raman D/G intensity ratio is proportional to the average size of the sp2 domains, the rise of the D/G intensity ratio was actually attributed to the increase in number of small in-plane sp2 domains, confirming the effectiveness of the conventional reduction.

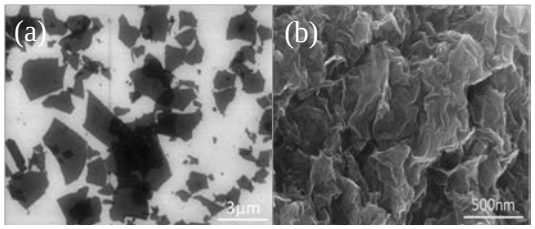

Fig. 4 SEM images of (a) rGO sheets from reduced, chitosan-containing solution, and (b) GO reduced with no additional dispersants.

SEM was utilized to analyze the dispersing state and morphology of the rGO in the suspension by dropping the suspension on silicon wafers. As shown in Fig.4, plentiful “transparent” separated rGO sheets appeared on the substrate, suggesting the rGO sheets in the suspension were well dispersed. In contrast, reduction of a GO without chitosan under a same condition produced black clusters which exhibited a highly agglomerated morphology in SEM. This indicates the chitosan played an important role for the dispersion of the rGO in water.

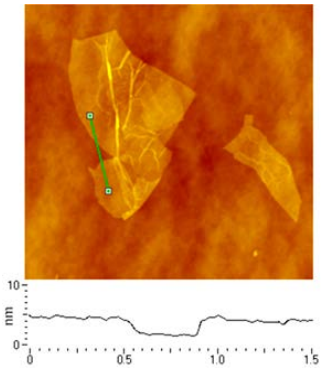

Fig. 5 AFM image of the rGO sheets from the chitosan-containing solution. The sample was rinsed by 0.1% HCl after deposition.

It is well known that, during reductions, GO gradually loses its oxygen-containing groups (OCGs) and becomes hydrophobic, so that direct reduction of GO in water without proper mediating agents generally causes irreversible aggregations. On the other hand, reduction of GO does not generate perfect graphene[12], and in the presence of chitosan, the residual OCGs of the rGO had the opportunity to capture the amino and hydroxyl groups of chitosan via zwitterionic interaction and hydrogen bonding and endowed with dispersibility in water. AFM showed that the rGO were about 3 nm in thickness (Figure 5), which is much thicker than GO (1.2nm) and the reported value for clean rGO (1 nm), indicating that there was a layer of chitosan anchored on the sides of the rGO sheets.

Chitosan is a weak polyelectrolyte and its molecular conformation and solubility can be reversibly altered by pH changes; therefore, noncovalent bonding of the rGO with chitosan offers the possibility of controlling the behaviors of the rGO in suspensions by using pH as a stimulus. For practical experiments, rGO/chitosan suspensions were tuned to different pH values (from 2 to 12) and their transmittances (at 500 nm) were recorded by a UV-vis spectrophotometer. The transmittances were plotted against the pH values (Figure 6a), which clearly shows a pH-dependent dispersibility of the rGO in the suspensions. Sharp transitions from dispersed to agglomerated states were observed when the pH changed from 6 to 7, which is consistent with ζ potential measurements (Fig. 6b).

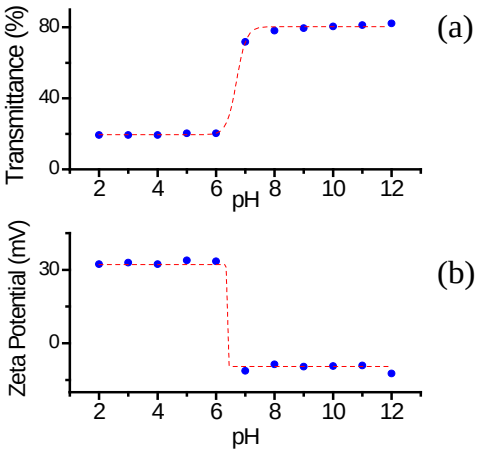

Fig. 6 (a) Transmittance of the supernatants of rGO/chitosan suspensions with different pH values after sedimentations. (b) Zeta potential of the rGO/chitosan suspension at different pH.

We also found that the agglomerated rGO can be redispersed when the suspension was tuned to acid conditions again, indicating that the dispersion/aggregation of the rGO in the suspension could be controlled by using pH change as a stimulus.

4. Conclusion

We demonstrate the preparation of homogeneous aqueous suspensions of grapheme, which is prepared by chemical reduction of GO in the presence of chitosan. The graphene in the suspensions can be reversibly switched between well-dispersed and aggregated states by changing the pH value. The study may serve as a prototype for future studies on using stimuli-responsive moieties to functionalize graphene for advanced applications.

Reference

[1] A.K. Geim and K.S. Novoselov, Nat. Mater. **6** (2007) 183.

[2] C. Lee, X. Wei, J.W. Kysar, and J. Hone, Science **321** (2008) 385.

[3] K.I. Bolotin, K.J. Sikes, Z. Jiang, M. Klima, G. Fudenberg, J. Hone, P. Kim, and H.L. Stormer, Solid State Commun. **146** (2008) 351.

[4] A.A. Balandin, S. Ghosh, W. Bao, I. Calizo, D. Teweldebrhan, F. Miao, and C.N. Lau, Nano Lett. **8** (2008) 902.

[5] K.S. Novoselov, A.K. Geim, S. V Morozov, D. Jiang, Y. Zhang, S. V Dubonos, I. V Grigorieva, and A.A. Firsov, Science **306** (2004) 666.

[6] X. Li, W. Cai, J. An, S. Kim, J. Nah, D. Yang, R. Piner, A. Velamakanni, I. Jung, E. Tutuc, S.K. Banerjee, L. Colombo, and R.S. Ruoff, Science **324** (2009) 1312.

[7] S. Stankovich, D.A. Dikin, R.D. Piner, K.A. Kohlhaas, A. Kleinhammes, Y. Jia, Y. Wu, S.T. Nguyen, and R.S. Ruoff, Carbon **45** (2007) 1558.

[8] S. Stankovich, R.D. Piner, X. Chen, N. Wu, S.T. Nguyen, and R.S. Ruoff, J. Mater. Chem. **16** (2006) 155.

[9] X. Li, X. Wang, L. Zhang, S. Lee, and H. Dai, Science **319** (2008) 1229.

[10] S. Park, N. Mohanty, J.W. Suk, A. Nagaraja, J. An, R.D. Piner, W. Cai, D.R. Dreyer, V. Berry, and R.S. Ruoff, Adv. Mater. **22** (2010) 1736.

[11] W.S. Hummers and R.E. Offeman, J. Am. Chem. Soc. **80** (1958) 1339.

[12] D. Li, M.B. Müller, S. Gilje, R.B. Kaner, and G.G. Wallace, Nat. Nanotechnol. **3** (2008) 101.

[13] M.S. Dresselhaus, A. Jorio, M. Hofmann, G. Dresselhaus, and R. Saito, Nano Lett. **10** (2010) 751.

Growth of Ca Silicide Layers by Thermal Treatment of Si Substrates in Ca Vapor

Yusuke Sato[*1]

[1] Faculty of Engineering, Shizuoka University, Hamamatsu, Shizuoka, Japan

[*] e-mail: f0911064@shizuoka.ac.jp

Abstract

Ca silicide layers were formed by thermal treatment of Si substrates in Ca vapor. I examined the difference in structure of two samples, which were synthesised by different growth time. The structural properties of the resultant composites were characterized by field emission scanning electron microscopy (FE-SEM) and X-ray energy dispersive spectroscopy (EDS).

1. Introduction

Recently, semiconducting silicides have attracted much attention for their potential to create new classes of environmentally conscious electronics. Silicon-based nanoscale materials, such as nanotubes, nanowires, and nanoparticles, have remarkable electronic and optical properties and are suitable for nanodevice applications owing to their extraordinary structures.

While zero- or one-dimensional nanomaterials may be suitable for nanoscale fabrication, two-dimensional nanomaterials can bridge the gap between the quantum world and three-dimensional bulk because of their nanoscale thickness and microscale area. To synthesize two-dimensional nanomaterials, chemical exfoliation is performed artificially for several classes of layered materials by certain soft-chemistry procedures. In adition, many researchers have attempted to prepare two-dimensional silicon sheets, there have been no reports of a successful fabrication of silicon monolayer sheets.

One of the method for silicon monolayer sheets synthesis, it is chemical exfoliation of calcium disilicide [1]. Therefore, as a first step for synthesized silicon monolayer sheets, we have a purpose of growth of Ca silicide layers by thermal treatment of Si substrates in Ca vapor.

2. Experiment

First, we prepared Ca ball (99.5 %, 1-3 mm) and Si (111) substrate. Ca ball was adjusted to be 0.05 grams. The Si (111) substrate was etched in HF solution (HF:HNO3:CH3COOH = 1:2:1) and rinsed with deionized H2O. Next, the substrate was immersed in a diluted hydrofluoric acid solution (HF:H2O = 1:9). Then Ca ball and Si substrates were located in a loosely sealed quartz container, which was loaded into a vacuum chamber. Then the container was heated up and the temperature was maintained at 600ºC.

During the heat treatment, Si substrates were exposed to Ca vapor, after which Ca-Silicide layers were formed on the Si substrates. We synthesized two samples by changing the time for the heat treatment. One is the sample(a) of the growth time of 15 minutes. The other one is the sample(b) of the growth time of 30 minutes.

The structural properties of the resulting structures were characterized by X-ray diffraction (XRD), field emission scanning electron microscopy (FE-SEM) and X-ray energy dispersive spectroscopy (EDS).

3. Results and Discussion

Figure 1 shows the SEM images of sample(a) and sample(b). And Table 1 shows results of EDS analysis of sample(a) and

Table 2 shows results of EDS analysis of sample(b).

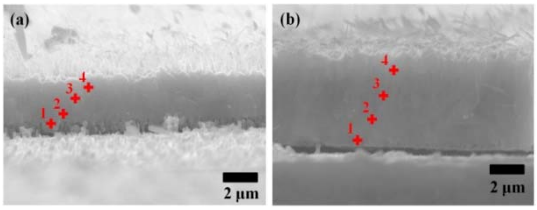

Fig.1 : SEM image of sample(a) (growth time:15 min) and sample(b) (growth time:30 min).

Table1 EDS analysis of sample(a)

Position at(%)	Ca	Si
1	37.79	62.21
2	49.04	50.96
3	61.85	38.15
4	63.05	36.95

Table2 EDS analysis of sample(b)

Position at(%)	Ca	Si
1	33.38	66.62
2	46.98	53.02
3	48.00	52.00
4	49.13	50.87

From figure1, We confirmed that the layer was synthesized on a Si substrate. And we can be confirmed that the sample(b) is thicker than sample(a). In addition, from table1and table2, the layer can be seen that it is composed of Ca and Si. Therefore, We considered the calcium silicide has been synthesized on a Si substrate.

From sample(a) and sample(b), we can be confirmedthat the atomic ratio of Ca to Si is approximately 1:2 near the boundary of the substrate and layer. We considered another material has been synthesized in the lower layer and the upper layer of the layer.

4. Conclusion

We tried synthesized Ca silicide on Si substrates. As a result, Ca silicide had synthesised by thermal treatment of Si substrates in Ca vapor. In addition, we considered another material has been synthesized in the lower layer and the upper layer of the layer. In future, to find the optimum growth time and growth condition for synthesis Ca silicide.

5. Reference

[1] Hideyuki Nakano, Takuya Mitsuoka, Masashi Harada,Kayo Horibuchi, Hiroshi Nozaki, Naoko Takahashi,Takamasa Nonaka, Yoshiki Seno, and Hiroshi Nakamura Angew. Chem. Int. Ed. 2006, 45, 6303 –6306

Thermal Annealing of Si_3N_4 with Gallium

Naoki Yamamoto

Faculty of Engineering, Shizuoka University
3-5-1 Johoku, Naka-ku, Hamamatsu, Shizuoka 432-8561, Japan
TEL&FAX: +81-53-478-1099
E-mail: f0711151@ipc.shizuoika.ac.jp

Abstract

Thermal annealing of Si_3N_4 with gallium in a nitrogen gas atmosphere. Wire is generated on the upper surface of the gallium. The structural properties of the resultant composites were characterized by field emission scanning electron microscopy (FE-SEM), and X-ray diffraction (XRD).

1. Introduction

Recently, gallium nitride attracts much attention in various fields. For example, it is used in car headlights and signal using a light-emitting diode. This is a material necessary to the present life, which is to enrich life. Other than a light-emitting diode, the application to a high power transistor solar battery is expected.

In addition, Photon Enhanced Thermionic Emission (PETE) was an opportunity to begin the study.[1] Photon Enhanced Thermionic Emission is a newly proposed form of solar energy harvesting which relies upon a combination of quantum and thermal processes to generate electricity. While minimizing costs and integration with existing infrastructure solar, PETE module can increase the power generation efficiency in a practical scale. Thus, it is possible to reduce the cost of power generation.

The purpose of this study, gallium nitride will be prepared by a simple way, and making a cheap solar battery.

2. Experimental

The composites were synthesized from liquid gallium (purity 99.99%) and silicon nitride powder (Si_3N_4). Silicon nitride was so as to be covered by the gallium at this time.

Synthesized sample was heated at 900ºC for 5 hours in an electric furnace. Electric furnace was filled with nitrogen when heated.

The structural properties of the resulting structures were characterized by X-ray diffraction (XRD), field emission scanning electron microscopy (FE-SEM).

3. Results and Discussion

Figure 1 shows the appearance of the sample after heat treatment. Wire had grown from the surface of the sample.

Figure 1, Appearance of the sample

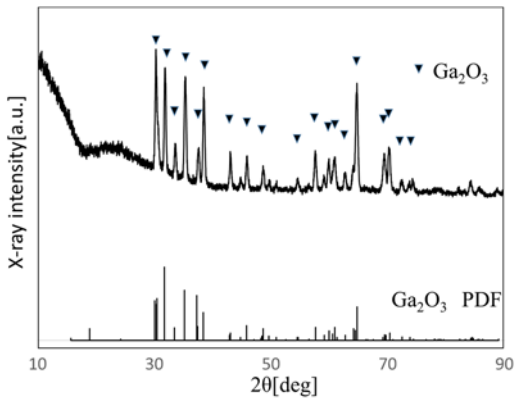

Figure 2, XRD spectrum of the sample

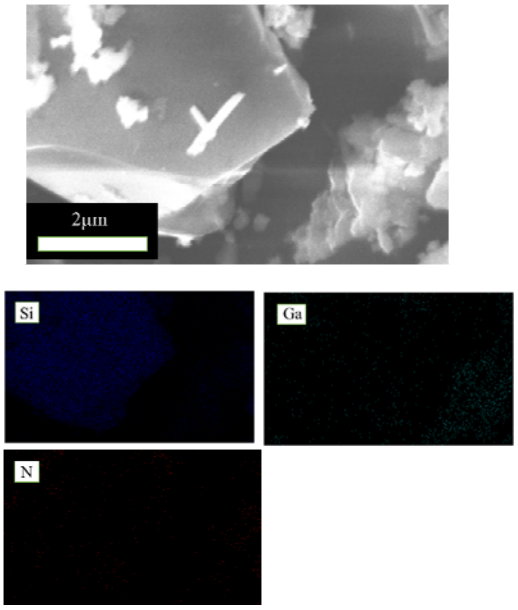

Figure 3, SEM image and EDS analysis of the sample

Figure 2 shows XRD spectrum of part of the sample. Ga2O3 was included in the sample from the result. However, GaN was not included in the sample from the result.

Figure 3 shows SEM image and EDS analysis of the sample. It is possible that nitrogen is lost from the silicon nitride from the results of EDS. As a result, it is considered that it has changed to the silicon.

4. Conclusion

Gallium and silicon nitride were heated at 900ºC for 5 hours in an electric furnace. Wires are grown on the surface of the sample. Ga_2O_3 was generated from the results of XRD.

GaN was not able to be formed on this experiment condition. Therefore, it is necessary to examine the growth temperature and the growth time GaN is generated in the future.

5. Reference

[1] Nicholas Melosh. Zhi-Xun Shen
Photon Enhanced Thermionic Emission for Solar Energy Harvesting
April 20, 2012

Deposition of Silicide-based Microstructures on Ca-silicide/Si substrates

Kaito Nakane[*1]
[1]Graduate School of Engineering, Shizuoka University, Hamamatsu, Shizuoka, Japan

[*]e-mail: f0230119@shizuoka.ac.jp

Abstract

Various Silicide-based microstructures were formed by $CrCl_2$ treatment of Ca-silicide/Si substrates. The $CrCl_2$ treatment time affects the structural property of micro/nano -structures. The structural properties of the resultant composites were characterized by field emission scanning electron microscopy (FE-SEM) and X-ray energy dispersive spectroscopy (EDS).

1. Introduction

Recently, semiconducting silicides, which consist of non-toxic and abundant materials at low cost, have attracted much attention for their potential to create new classes of environmentally conscious electronics. In addition, low-dimensional materials have attracted much interest due to their enhanced or modified optical, electronic and mechanical properties compared to those of bulk materials.

It has been reported that synthetic method of the silicon nano sheet which used pure Cl_2 and Metal-chlorides, such as $SbCl_3$, $FeCl_3$, S_2Cl_2, PCl_5, $SnCl_2$, however, the structures of the sheets have not been clarified yet [1-2]. Using metal chlorides, the formation of silicides and silicon nanostructures and their structural modification have been intensively investigated. $CrCl_2$ is one of appropriate metal chlorides source materials to synthesize silicide nanostructures [3].

This paper shows Synthesis of micro-/nano-structures by CrCl2 treatment of Ca - silicide/Si substrates. The structural properties of micro/nano -structures were investigated.

2. Experimental

First, we prepared Ca-silicide/Si substrates with starting materials of Ca ball (99.5 %, 1-3 mm) and Si (111) substrate. Ca ball and Si substrates were located in a loosely sealed quartz container, which was loaded into a vacuum chamber. Then the container was heated up and the temperature was maintained at 600ºC. During the heat treatment, Si substrates were exposed to Ca vapor, after which Ca-Silicide layers were formed on the Si substrates.

For the $CrCl_2$ treatment, the reaction apparatus was flushed with argon gas to remove any oxygen and moisture in the furnace. After the furnace reactor was heated, then the Ca-silicide/Si substrates and 0.08 g of the $CrCl_2$ source materials were placed in the reactor. The $CrCl_2$ source material was evaporated at 872 ºC, then reacted with the Ca-silicide/Si substrates in the range of 650 ºC and maintained for 2 - 15 min, then cooled to room temperature without the flow of argon gas [3].

The morphological and structural properties of the resulting structures were characterized by X-ray diffraction (XRD), field emission scanning electron microscopy (FE-SEM) and X-ray energy dispersive spectroscopy (EDS).

3. Results and Discussion

Figure 1 shows the SEM images of Sample grown at 2 min $CrCl_2$ treatment. From figure 1(a), it is found that large quantity of white nanostructures were deposited on the sample surface. In addition, white nanoparticles 0.5-0.8 μm in diameter can be observed, as show in the Fig.1 (b). Moreover, it is found that microwires were grown with nanoparticles.

Figure 2 and Table 1 shows results of SEM image and EDS analysis of Sample

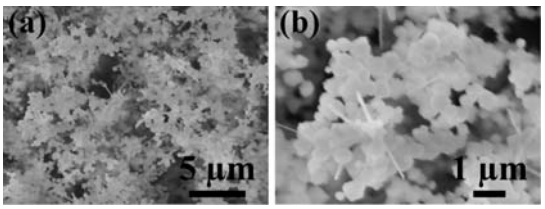

Fig. 1. SEM image of nanoparticles ($CrCl_2$ treatment time:2min)

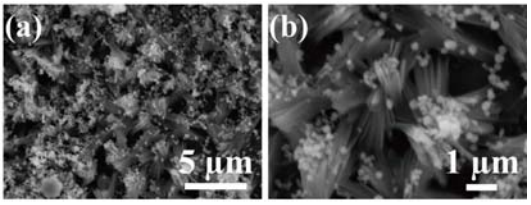

Fig. 3. SEM image of microrods ($CrCl_2$ treatment time:15 min)

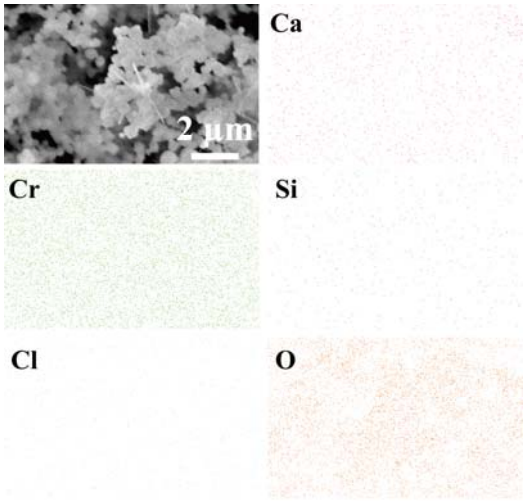

Fig. 2. SEM image and corresponding EDS mappings of the nanoparticles grown at 650 ºC, 2 min $CrCl_2$ treatment

Table1 EDS analysis

Element	Ca	Si	Cr	Cl	O
[at%]	3.12	0.60	39.50	0.56	56.21

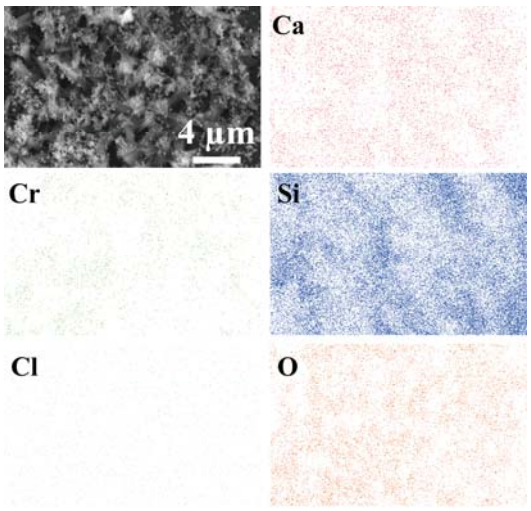

Fig. 4. SEM image and corresponding EDS mappings of the microrods grown at 650 ºC, 15 min $CrCl_2$ treatment

Table2 EDS analysis

Element	Ca	Si	Cr	Cl	O
[at%]	6.01	36.47	7.13	6.91	43.47

grown at 2 min $CrCl_2$ treatment. This result shows that the composition of the nanoparticles were mainly consist of Cr and O.

Figure 3 shows the SEM images of Sample grown at 15 min $CrCl_2$ treatment. As shown in Fig.3 (a), a large number of microrods were formed on the sample surface. From figures 1(b), microrods 3-4 μm in length and nanoparticles were observed. In addition, it is found that wires are bundle. Moreover, nanoparticles were located on the surface of the nanorods and on the top of the wires.

Figure 4 and Table 2 shows results of SEM image and EDS analysis of Sample grown at 15 min $CrCl_2$ treatment. This result shows that the composition of the microwires is mainly consist of Si and O.

4. Conclusion

Compites with various micro-/nano-structures were synthesized by CrCl2 treatment of Ca-Silicides/Si substrate. The $CrCl_2$ treatment affect the structural property of resulting comppsotes.

In future, Well-aligned silicide-based micro- /nano-structures will be grown and their electrical and optical characterizations will be expected.

Reference

[1] H. Kautsky and L. Haase, Chem. Ber. 86 (1953)1226

[2] E. Bonitz, Chem. Ber. 94(1961)220
[3] W. Li, E. Meng, T. Matsushita, S. Oda, D. Ishikawa, K. Nakane, J. Hu, S. Guan, A. Ishida and H Tatsuoka, J. Cryst. Growth 365(2013)11

Synthesis of Si nanowires using $MnCl_2$ and Si powders source on Si substrate with Au catalyst

Erchao Meng*

Graduate School of Science and Technology, Shizuoka University, 3-5-1 Johoku, Naka-ku, Hamamatsu 432-8011, Japan

TEL: +81-53-478-1099, Fax: +81-53-478-1099
E-mail: f5145034@ipc.shizuoka.ac.jp

Abstract

High-density and high-quality Si nanowires were synthesized using $MnCl_2$ and Si powder on the Si substrates with Au catalyst. As comparison, under the same growth condition, when Si powder was used as source materials, there was no nanowires grown. The Si nanowires grown are characterized by SEM, TEM and STEM with EDS.

1. Introduction

Recently, novel devices, based on nano-materials, have attracted a great deal of attention because of their potentials for many industrial applications. Therefore, the huge efforts have been devoted to nanomaterials researches. Si nanowries have good potentials for application, thus, which have been synthesized by many methods such as chemical vapor deposition [1] and high temperature thermal evaporation [2, 3]. On the other hand, many kinds of Si precursors were used for Si nanowires growth such as SiH4 and Si2H6, and so on [4]. However, for these growth methods and Si precursor, usually complex processes, the toxic and dangerous precursor gases or the high reaction temperature are needed. Therefore, it is necessary to develop a new synthesis method of Si nanowires.

In this study, Si nanowires were synthesized using $MnCl_2$ and Si powder as source materials on the Si substrate, and Au is used as catalyst for Si nanowries growth.

2. Experiments

The nanowires were synthesized on Si(111) substrates. The Si(111) substrates was degreased with solvent, etched in HF solution ($HF:HNO_3:CH_3COOH$ = 1:2:1) and rinsed with deionized H2O. Next, the substrates were immersed in a diluted hydrofluoric acid solution ($HF:H_2O$ = 1:9), and then dried prior to loading into a vacuum for Au deposition. The Si substrates were prepared with Au deposition with the thickness of about 3 nm as a catalyst.

On the other hand, $MnCl_2$ and Si powders with a mole ration of 1:3 were used as source materials. The Si substrates and the source materials were located in a loosely sealed quartz container, which was loaded into a vacuum chamber. Then the camber was pumped down to a base pressure of 10^{-3} Pa. Then the container was heated up and the temperature was maintained at 700-850 □ for 60 min. A schematic illustration of the growth equipment used in this study was shown in Ref. [5].

The morphological and structural properties of the resultant nanostructures were characterized by scanning electron microscopy (SEM) with energy dispersion spectroscopy (EDS), transmission electron microscopy (TEM) and scanning transmission electron microscopy (STEM) with EDS.

3. Results and Discussion

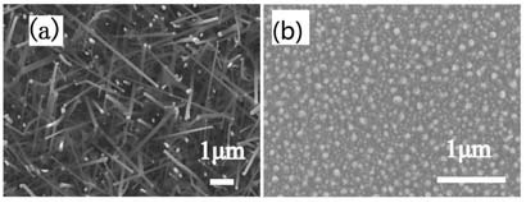

Figure 1 SEM images of the resultant products synthesized using (a) MnCl2 and Si powder source (b) Si powder source

Figure 1(a) shows SEM image of Si nanowires, which were synthesized using $MnCl_2$ and Si powder source on the Si substrates with Au catalyst. The source and substrate temperatures were maintained for 1 h at 850 and 700 □. As comparison, Figure 1(b) shows SEM image of the resultant product synthesized using Si powder under the same growth condition.

From SEM images, it can be seen that when using $MnCl_2$ and Si powder as source materials, Si nanowires with high-density and high-quality were grown on the Si substrates. However, using Si powder source, just some particles were grown on the Si substrate, no nanowires were observed. The results indicated that $MnCl_2$ plays an important role in fabricating Si nanowires.

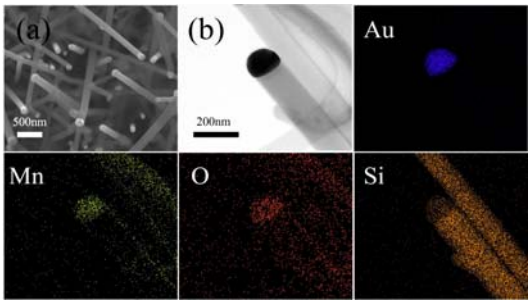

Figure 2 SEM, STEM images and EDS mappings of the Si nanowires grown on the substrate with Au catalysts using $MnCl_2$ and Si powder source.

Figure 2 shows the SEM, STEM images and EDS mappings of the Si nanowires grown on the substrate with Au catalysts using $MnCl_2$ and Si powder source. Figure 2(a) shows the conventional columnar Si nanowires with high-density were grown, and the catalyst particles can be clearly observed on the top of Si nanowires. The STEM image in Figure 2(b) shows that the surface of Si nanowires is smooth, and the diameter of nanowires is almost the same as that of catalyst particles on the top of nanowires.

EDS mapping shows that Si was distributed on the entire nanowire, while Au was mainly concentrated in the top of nanowire, which suggested that Si nanowires were synthesized by Au catalyst via VLS growth mechanism. It is also observed that oxygen and manganese atoms were detected in the catalyst particle, and few oxygen is detected in the nanowire. Manganese atoms is adsorbed into Au-Si solution, and is oxidized, which suppressed the oxidation of Si nanowires.

Figure 3 shows TEM image, HRTEM image and the corresponding FFT pattern of Si nanowires, which were synthesized using $MnCl_2$ and Si powder as the source materials. TEM image shows that the straight and smooth surface Si nanowires with hemispherical catalyst particles on the top of nanowires were grown. HRTEM image shows that the lattice spacings between two neighboring fringes measured are 0.331nm and 0.201nm, and the angle between these two planes is 35º, which corresponds to those of the (111) and (220) planes of Si. It demonstrated that Si nanowires were synthesized, which is consistent with the mapping result shown in Figure 2. The corresponding FFT pattern indicated that Si nanowire was grown along the [111] direction.

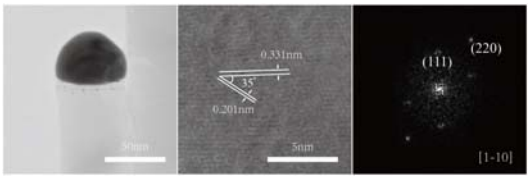

Figure 3 TEM image, HRTEM image and the corresponding FFT pattern of Si nanowires synthesized using $MnCl_2$ and Si powder source on the Si substrate with Au catalyst.

It is reported that when Si powder was used as raw materials for growth of silicon nanowires, the evaporation temperature of source materials used in experiments is more than 1000□ in order to fabricate Si nanowires [6]. However, here in our study, the source temperature is 850□ (actually, according to our experimental results, Si nanowires can be fabricated at lower source temperature), which is lower than the evaporation temperature of Si powder. Thus, Si powder can not be evaporated, and there is no nanowires grown on the Si substrate, as shown in Figure1(b).

4. Conclusions

High-density and high-quality Si nanowires were synthesized using $MnCl_2$ and Si powder on the Si substrates with Au catalyst at lower source temperature comparing with Si powder source. This simple and low-cost growth technique is expected to be applied to other semiconductor nanostructures.

References

[1] Nong M. Hwang, Woo S. Chenong, Duk Y Yoon and Doh-Y. Kim, Journal of Crystal Growth 218 (2000) 33.
[2] Y. Shi, Q. Hu, H. Araki and T. Noda et al., Applied Physics A, 80 (2005) 1733.

[3] A. Colli, A. Fasoli, P. Beecher and J. Robertson et al., Journal of Applied Physics 102 (2007) 034302.
[4] W. Molnar, A. Lugstein, P. Pongratz, N. Auner, C. Bauch and E. Bertagnolli, Nano Lett. 10 (2010)3957-3961.
[5] Y. Mizuyoshi, R. Yamada, T. Ohishi, Y. Saito, T. Koyama, Y. Hayakawa, T. Matsuyama and H. Tatsuoka, Thin Solid Films 508 (2006)70.
[6] Y. Shi, Q. Hu, H. Araki, H. Suzuki, H. Gao, W. Yang and T. Noda, Applied Physics A, 80(2005) 1733-1736.

Effect of Nickel Addition on Growth Evolution of Silicon Nanostructures using $MnCl_2$ and Si powders

Hiroaki Suzuki

Faculty of Engineering, Shizuoka University
TEL&FAX: 053-478-1099
E-mail: f0911042@ipc.shizuoka.ac.jp

Abstract

Faceted nanowires can be fabricated with Vapor-Liquid-Solid-Solid (VLSS) Growth Mechanism and square shape nanowire using Si powders and $MnCl_2$ as source is reported. In this paper, I added Nickel as impurity in the source and investigated the effect of Nickel addition.

1. Introduction

Thermoelectric device is generic name of the element, using a phenomenon to connect electricity with heat. For example power generator, heating and cooling applications.

Recently, attention has focused on the thermoelectric device as a power generator because of diverse reasons. For example, it can be small, doesn't need external source, etc. Therefore, thermoelectric device has been researched for a long time and improved efficiency.

The efficiency of thermoelectric material is represented by its dimensionless figure of merit, ZT, which is calculated by the following relational expression:

$$ZT = \frac{S^2 \sigma T}{\kappa_{lattice} + \kappa_{electronic}}$$

where S is the Seebeck coefficient, σ is the electrical conductivity, T is the temperature, and $\kappa_{lattice}$ and $\kappa_{electronic}$ are the lattice and electronic contributions to the thermal conductivity, respectively. In this expression, Seebeck coefficient, electrical conductivity and electronic thermal conductivity have influences each other, but only lattice thermal conductivity doesn't have relation with other parameters because it depends on phonon although others depend on electron. It means that, to lower the lattice thermal conductivity makes high ZT and to change the structure can make low lattice thermal conductivity.

The fabrication of faceted square nanowire with Vapor-Liquid-Solid-Solid (VLSS) Growth Mechanism using Si powders and $MnCl_2$ as source is reported [1]. Therefore in this paper I aim at the investigation of the effect of Nickel addition to the source.

2. Experiment

The Si nanostructures were synthesized on Si (111) substrates. The Si (111) substrates was degreased with solvent, etched in HF solution ($HF:HNO_3:CH_3COOH$ = 1:2:1) and rinsed with deionized H_2O. Next, the substrates were immersed in a diluted hydrofluoric acid solution ($HF:H_2O$ = 1:9), and then dried prior to loading into a vacuum for Au deposition. The Si substrates were prepared with Au deposition with the thickness of about 3 nm as a catalyst.

On the other hand, Si powders, $MnCl_2$ and Ni with a mole ration of 1:1:0.1 and 1:1:0.02 were used as source materials. The Si substrates and the source materials were located in a loosely sealed quartz container, which was loaded into a vacuum chamber. Then the camber was pumped down to a base pressure of 10^{-3} Pa. Then the container was heated up and the temperature was maintained at 700-900 ^oC for 25min.

The structural properties of the resultant nano/microstructures were characterized by scanning electron microscopy (SEM).

3. Results and Discussion

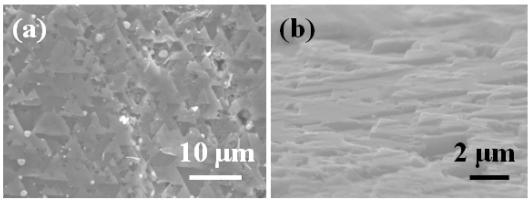

Fig. 1 SEM images of (a) plan-view and (b) angle images (source materials mole ration = 1:1:0.1)

Figure 1 shows SEM images of plan-view and angle images (source materials mole ration = 1:1:0.1). In this figure, I observed triangular structures on the surface. And the height of structures was approximately 1 μm.

From this result, I thought Ni had a large effect. So next experiment, I used less Ni.

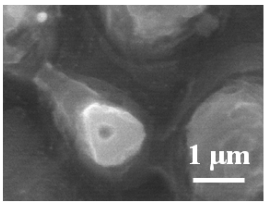

Fig. 2 SEM images of plan-view images (source materials mole ration = 1:1:0.02).

Figure 2 shows SEM images of plan-view images (source materials mole ration = 1:1:0.02). I found triangle-like hexagonal microrods this time.

From the last result of triangle structures and microrods at this time, possibly we can get triangle nanowires.

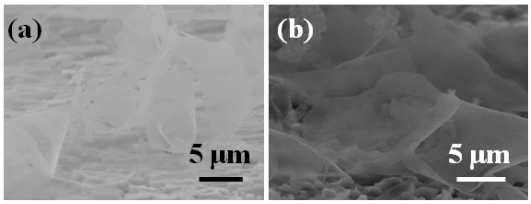

Fig. 3 SEM images of angle images. Source materials mole ration = 1:1:0.1 (a), 1:1:0.02 (b).

And in these experiments, I came across the nanosheets. Figure 3 shows SEM images of nanosheets with source materials mole ration of (a) 1:1:0.1, (b) 1:1:0.02. If we use Si powders and $MnCl_2$ as source, we can hardly get the nanosheet.

4. Conclusions

I investigated effect of Nickel Addition on Growth Evolution of Silicon Nanostructures using $MnCl_2$ and Si powders. Triangle and triangle-like hexagonal microstructures were fabricated, but nanowires can't be found. And at the same time, I came across some nanosheets.

In the future, I want to clarify the mechanism of effect of Ni addition and control nanostructures.

References

[1] E. Meng, W. Li, K. Nakane, Y. Shirahashi, Y.Hayakawa, and H. Tatsuoka, AIP Advances 3, 092107 (2013)

Nitric acid treatment of $MoSi_2$ Nanosheets synthesized by Molten Salt Technique using MoS_2

Daisuke Ishikawa

Graduate School of Engineering, Shizuoka University,
3-5-1 Johoku, Naka-ku, Hamamatsu 432-8561, Japan
E-mail tehtats@ipc.shizuoka.ac.jp

Abstract

The hexagonal phase $MoSi_2$ was formed by the molten salt technique using MoS_2 powder as the source material. Nitric acid treatment was performed to the resultant silicides. The structural and morphological properties of the resultant silicides are characterized. The layered structure of MoS_2 with a hexagonal crystalline structure would affect the growth morphology and enhance the formation of the hexagonal $MoSi_2$. Moreover, Synthesis of the h-$MoSi_2$ was promoted by adding S atom. Impurities decreased by performing Nitric acid treatment.

1. Introduction

Recently, semiconducting silicides, which consist of non-toxic and abundant materials, have attracted much attention for their potential to create new classes of environmentally conscious electronics [1]. The group VI metal silicides are classified in this material group [2]. $MoSi_2$ with stable tetragonal (t-) phases is metallic and has been used in electrode wire materials. The t-$MoSi_2$ has lattice constants of a=0.3205 nm and c=0.7845 nm. On the other hand, the hexagonal (h-) phase $MoSi_2$ has lattice constants of a=0.4622 nm and c=0.6646 nm, and is known to be a narrow gap semiconductor. It is reported that the low temperature phase, h-$MoSi_2$, is expected to be one of the novel silicide semiconductors, which has improved thermoelectric properties [2]. However, the electrical and thermoelectric property of the bulk crystal h-$MoSi_2$ have not been experimentally clarified. Since t-$MoSi_2$ is transformed into h-$MoSi_2$ with the Ti addition by a Mechanical Alloying (MA) technique in the Mo-Ti-Si system [3], it has been reported that Mo-silicides were grown using Mo substrates and Mo-Ti alloy (Mo(Ti)) compacts by the molten salt method. However, the tetragonal phase was formed as well as the hexagonal phase in the silicides. A nonhomogeneous compositional distribution of Mo and Si atoms was observed in the silicides when using the Mo substrate and Mo(Ti) compact [4]. The single phase growth of h-$MoSi_2$ and improved compositional homogeneity of the silicide are required.

On the other hand, MoS_2 has a hexagonal structure with lattice constants of a=0.31612 and c=1.22985 nm. The detailed structure of MoS_2 and extraordinary chemical properties of the two-dimensional MoS_2 nanoclusters are described in Refs.5 and 6, respectively. MoS_2 has a characteristic layered structure, i.e., metal chalcogenide slabs are formed by two layers of close-packed chalcogenide atoms sandwiching one metal layer between them. These slabs are stacked with only van der Waals forces between the slabs [7]. It is considered that the use of the thin separated slabs would improve the homogeneity of the atomic distribution in the resultant alloys, because the diffusing species easily can pass through the materials during the treatment. Moreover, it has also been reported that the crystalline structure of the resultant compounds is strongly affected by that of the starting materials. For example, the formation of the zincblende-MnTe phase was demonstrated using ZnTe [8]. Single phase Ca_2Si was obtained using Mg_2Si as the starting material [9]. In the same manner, it is expected that the h-$MoSi_2$ would be easily obtained using MoS_2 as the source material. Moreover, MoS_2 has layered structures. It is expected $MoSi_2$ synthesized by Molten salt technique by using MoS_2 have

nanostructures. Nanostructures have unique properties and novel applications compared to those of bulk materials. A decrease in the thermal conductivity and an increase in the power factor, σS^2, of the nanostructures have been demonstrated by the theoretical calculations and proof of principle experiments, relative to the corresponding bulk structures.[10-13]

In this study, the synthesis of h-$MoSi_2$ was examined using MoS_2 powder. In order to remove impurities, Nitric acid treatment was performed. The structural and morphological properties of the resultant silicides were also characterized.

2. Experiments

The Mo-silicide powder was synthesized using MoS_2 powder, S powder and a molten salt, comprised of 36.58 mol%NaCl - 36.58 mol%KCl - 21.95 mol%NaF - 4.89 mol%Na_2SiF_6. The salt mixture, silicon powder (99.999%, 21.85 mol% for the salt mixture), S powder (99.99 %, 10 mol% for salt mixture) and MoS_2 powder (99.9%up, 2.73 mol% for salt mixture) were placed in an SiO_2–Al_2O_3 crucible with the powder. They were thermally treated at 873 and 973K. After the heat treatment, the salt was removed from the sample using deionized H_2O. Then, Nitric acid treatment was performed to the sample. Figure.1 shows Nitric acid treatment process. The structural p roperties of the powder were characterized by X-ray diffraction (XRD) and transmission electron microscopy (TEM).

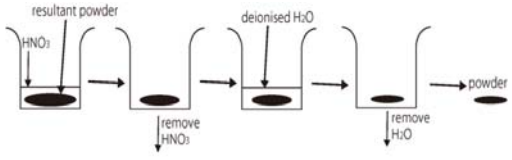

Fig.1 Nitric acid treatment process

3. Results and Discussion

Figure.2 shows the intensity ratio of MoS_2(002) and $MoSi_2$(111) by XRD spectra of the resultant powder by using S and MoS_2 as the source material at 600 ºC and 700 ºC. Synthesis of the h-$MoSi_2$ was promoted by adding S powder.

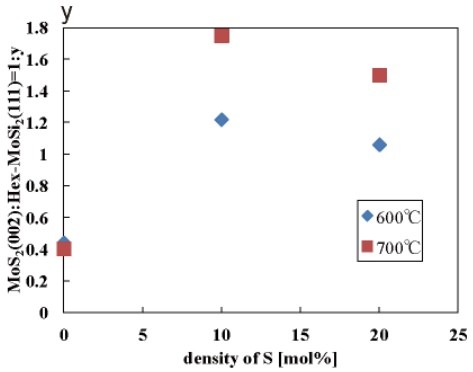

Fig.2 Intensity ratio of MoS_2(002) and $MoSi_2$(111) by XRD spectra of the resultant powder by using S and MoS_2 as the source material at 600 ºC and 700 ºC.

Figure.3 shows a TEM image of the resultant powder using MoS_2 as the source material. As shown in Fig.3, plate like structures were grown, which is due to the layered structure of the MoS_2 as source material.

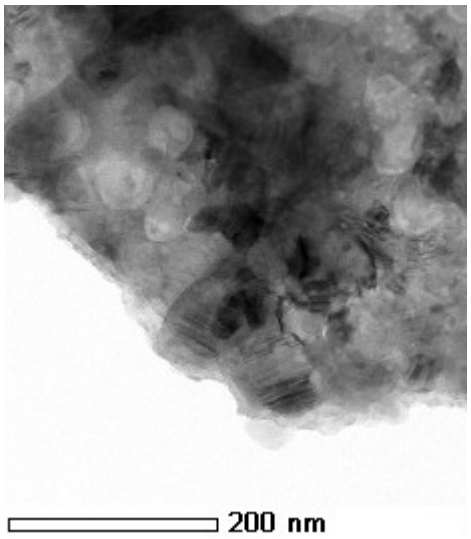

Fig.3 TEM image of the resultant powder using MoS_2 as the source material at 600 ºC / 4h.

Figure.4 shows XRD spectra of Nitric acid treatment performed to the resultant powder by using MoS_2 as the source material at 600 ºC. After Nitric acid treatment, the number of peaks of impurities decreased.

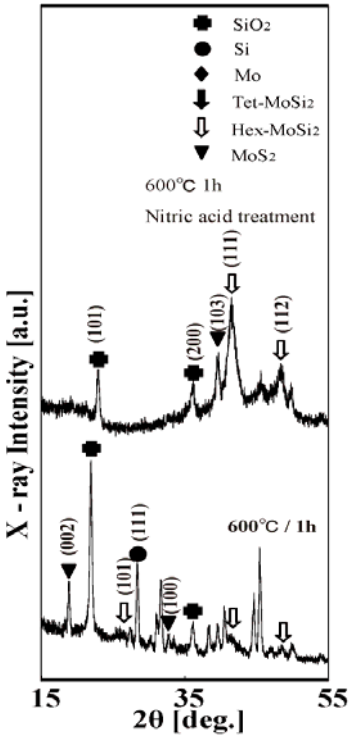

Fig.4 XRD spectra of the resultant powder by using MoS_2 as the source material at 600 ºC after Nitric acid treatment.

4. Conclusion

The h-$MoSi_2$ was grown using MoS_2 powder as the source material by the molten salt method. Moreover, thin silicide firms were synthesized. Synthesis of the h-$MoSi_2$ was promoted by adding S atom. It is expected that this simple growth procedure to fix the crystalline structure using the appropriate starting material. Impurities decreased by performing Nitric acid treatment.

Acknowledgements

I would like to thank K. Nakane and H.Koyama and H. Tatsuoka for their fruitful discussions.

Reference

[1] APAC-SILICIDE, July 29-31, 2006, Kyoto, Thin Solid Films **515**(22), pp. 8101-8300, edited by Y. Maeda, K.P. Homewood, T. Sadoh, Y. Terai, K. Yamaguchi and K. Akiyama.

[2] T. Nonomura, C. Wen, A. Kato, K. Isobe, Y. Kubota, T. Nakamura, M. Yamashita, Y. Hayakawa and H. Tatsuoka, Physics Procedia **11**, 110 (2011).

[3] A. J. Heron and G. B. Schaffer, Mater. Sci. Eng. A**352**, 105 (2003).

[4] T. Nonomura, C. Wen, K. Shirai, K. Isobe, A. Kato, Y. Kubota, T. Nakamura, Y. Hayakawa and H. Tatsuoka, IOP Conf. Ser.: Mater. Sci. Eng. **18**, 14 (2010).

[5] L. S. Byskov, J. K. Norskov, B.S. Clausen, and H. Topsoe, J. Catal. **187**, 109 (1999).

[6] J. V. Lauriitsen, M. Nyberg, R.T. Vang, M.V. Bollinger, B.S. Clausen, H. Topsoe, K. W. Jacobsen, E. Laegsgaard, J. K. Norskov and F. Besenbacher, Nanotechnology **14**, *385* (2003).

[7] C. F. Castro-Guerrero, F. L. Deepak, A. Ponce, J. Cruz-Reyes, M. D. Valle-Granados, S. Fuentes-Moyado, D. H. Galván and M. Jose-Yacamán, Catal. Sci. Technol. **1**, 1024 (2011).

[8] T. Matsumoto, Y. Souno, H. Tatsuoka, Y. Nakanishi, H. Kuwabara, Appl. Surf. Sci. **169/170**, 325 (2001).

[9] T. Hosono, M. Kuramoto, Y. Matsuzawa, Y. Momose, Y. Maeda, T. Matsuyama, H. Tatsuoka, Y. Fukuda, S. Hashimoto and H. Kuwabara, Appl. Surf. Sci. **216**, 620 (2003).

[10] L. D. Hicks et al., Phys. Rev. B 47, 12727 (1993).

[11] L. D. Hicks et al., Phys. Res. B 47, 16631 (1993).

[12] R. Venkatasubramanian et al., Nature 413, 597 (2001).

[13] A. I. Hochbaum et al., Nature 451, 163 (2008).

Effect of Ca addition on microstructure, mechanical properties and degradation behavior of Mg–Zn–Sr alloy

Xiang Meng [a], Hirokazu Tatsuoka [b,] *, Shaokang Guan [c]

[a] Graduate School of Science and Technology, Shizuoka University, 3-5-1 Johoku, Naka-ku, Hamamatsu 432-8011, Japan
[b] Faculty of Engineering, Shizuoka University, 3-5-1 Johoku, Naka-ku, Hamamatsu, Shizuoka 432-8561, Japan
[c] Materials Research Center, School of Materials Science and Engineering, Zhengzhou University, Wenhua Road 97, Zhengzhou, Henan 450002, China
* E-mail: tehtats@ipc.shizuoka.ac.jp

Abstract

The effect of trace Ca addition on the microstructure, mechanical properties and degradation behavior of the as-cast Mg-2wt. % Zn-0.3wt. % Sr alloys was investigated in this study. The results indicated that there always were a decrease in grain size and an increase in strength with the increase of Ca content which were under 0.3wt%. Degradation was studied by using immersion tests in Hanks' solution. With more Sr addition the corrosion resistance of alloys declined.

1. Introduction

Magnesium (Mg) alloys have gained significant interests for their potential application as biodegradable and bio-absorbable implant materials [1, 2]. Unfortunately, the high degradation rate of Mg in physiological conditions is always a significant challenge to its application.

Element alloying is one of the effective measures to improve the mechanical properties and corrosion resistance of Mg alloys. For preventing or minimizing cytotoxicity or adverse tissue reactions, using of the alloying elements that exist in the human body or have been shown to have beneficial effects on tissue regeneration and healing can be beneficial. Such elements, like zinc (Zn), Calcium (Ca) and strontium (Sr) are non-toxic or less-toxic to human, which were chosen for investigation in this study. The content of Ca was changed in order to study its effect on microstructure, mechanical properties and in-vitro corrosion properties of Mg-Zn-Ca-Sr alloys.

2. Experimental

In the present study, Mg-2wt. %Zn- 0.3 wt. % Sr –x wt. % Ca (x=0, 0.1, 0.25, 0.5) alloys were prepared in a mild steel crucible under CO_2/SF_6 (volume fraction rate, 3000:1) atmosphere in an electronic resistance furnace. The microstructure of the specimens was observed by optical microscopy (Olympus, H2-UMA) and scanning electron microscopy (Philips, Quanta-2000). The tensile tests (69 mm × 25 mm × 5 mm) were carried out on an SHIMADZU（AG-1C）material testing machine. The potentiodynamic polarization experiments were conducted on an electrochemical workstation (RST5200).

3. Results and discussion

3.1. Microstructure

Fig. 1 shows the optical microstructures of the quaternary Mg–2wt. %Zn–0.3 wt. % Sr-x wt. % Ca (x = 0, 0.1, 0.25, 0.5) alloys. With the increase of Ca content, the grain size of alloys decreased gradually. This mostly can be attributed to the growth restriction by solute effect or by the nucleating particles as fine precipitates were observed in the grains and along grain boundaries [3].

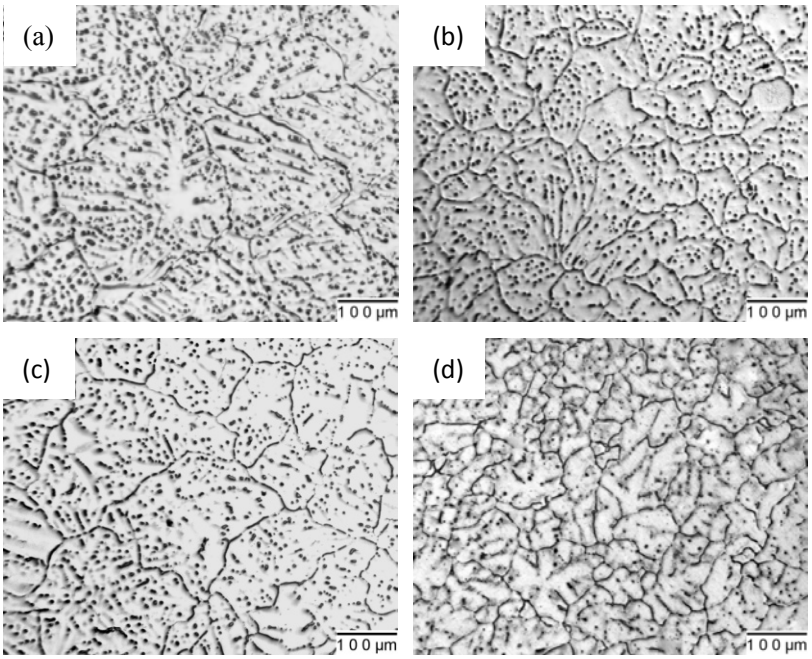

Fig. 1. Optical microstructures of alloys. (a) Mg-2Zn-0.3Sr alloy; (b) Mg-2Zn-0.3Sr-0.1Ca alloy; (c) Mg-2Zn-0.3Sr-0.25Ca alloy; (d) Mg-2Zn-0.3Ca-0.5Ca alloy.

3.2. Mechanical properties

Fig. 2 shows the mechanical properties of Mg-2Zn-0.3SrSr-x Ca alloys. It can be seen clearly that with the increasing Ca content, the tensile strength increased firstly and then decreased; Mg-2Zn-0.25Ca-0.3Sr alloy exhibited the highest tensile strength which was higher (24%) than Mg-2Zn-0.3Sr alloy. When the content of Ca was over 0.3 wt. %, trend of tensile strength obviously decreased.

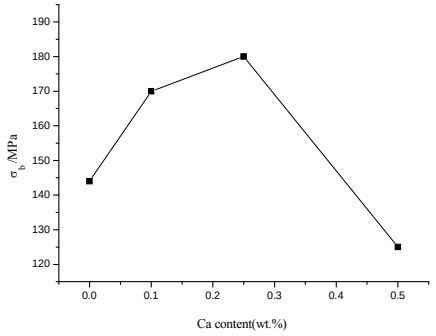

Fig. 2. Mechanical properties of Mg-Zn-Sr-x Ca alloys.

3.4. Immersion test

Fig. 3(a) illustrates the variation of pH value with immersion time in SBF for 72 h. More Ca addition brings more second phase, which lets alloys generate more Mg^{2+} ions which increased the pH values [4]. Fig. 3(b) shows the mass loss curves of different samples after immersion time in SBF solution at **37** □ for 120 h. It can be seen that the corrosion rate of the as-cast alloy was similar with the variation of pH value. Ca addition decreases the corrosion resistance of alloys, but not obviously.

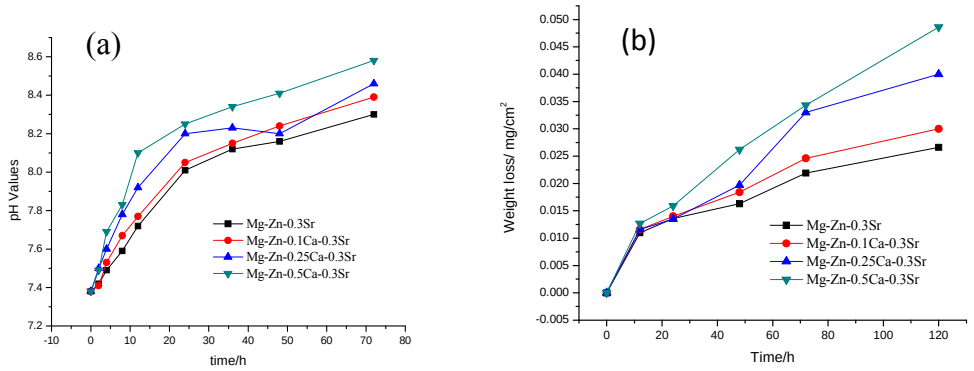

Fig. 3. (a) The pH values and (b) the mass loss curves of different samples with immersion time in SBF solution at 37 ℃.

4. Conclusion

The microstructural, mechanical properties and degradation behavior of Mg-Zn-Ca-Sr alloys were investigated. The Mg-2.0wt%Zn-0.25wt%Ca-0.3wt%Sr showed to be a promising biodegradable alloy candidate due to their low degradation rate and moderate mechanical properties. It is important to control the microstructure for optimization of both mechanical and degradation behavior of the alloys.

Reference

[1] Witte, F., Kaese, V., Haferkamp, H., Switzer, E., Meyer-Lindenberg, A., Wirth, C.J., Windhagen, H., 2005. In vivo corrosion of four magnesium alloys and the associated bone response. Biomaterials 26, 3557-3563.

[2] Brar, H.S., Keselowsky, B.G., Sarntinoranont, M., Manuel, M.V., 2011. Design considerations for developing biodegradable magnesium implants. JOM 63, 100-104.

[3] HUANG Xiao-feng, ZHU Kai, CAO Xi-juan. The Roles of Alloying Elements in Magnesium Alloys. Foundry Technology, 2008, 29(11), 1574-1578.

[4] Harpreet S. Brar, Joey Wong, Michele V. Investigation of the mechanical and degradation properties of Mg-Sr and Mg-Zn-Sr alloys for use as potential biodegradable implant materials. Journal of the Mechanical Behavior of Biomedical Materials, 7(2012): 87-95.

Sulfur Concentration Dependence on Structural Property of $MoSi_2$ Synthesized by Molten Salt Technique using MoS_2

Hajime Koyama

Faculty of Engineering, Shizuoka University

TEL&FAX: 053-478-1099

E-mail: f0911061@ipc.shizuoka.ac.jp

Abstract

The hexagonal phase MoSi2 was formed by the molten salt technique using MoS2 powder as the source material. And it is reported synthesis of the Hexagonal MoSi2 was promoted by adding S atom. In this paper, I investigated sulfur concentration dependence on structural property of MoSi2 synthesized.

1. Introduction

Recently, semiconducting silicides have attracted much attention for their potential to create new classes of environmentally conscious electronics. The group VI metal silicides are classified in this material group [1]. MoSi2 with stable tetragonal (t-) phases is metallic and has been used in electrode wire materials. The t-MoSi2 has lattice constants of a=0.3205 nm and c=0.7845 nm. On the other hand, the hexagonal (h-) phase MoSi2 has lattice constants of a=0.4622 nm and c=0.6646 nm, and is known to be a narrow gap semiconductor. It is reported that the low temperature phase, h-MoSi2, is expected to be one of the novel silicide semiconductors, which has improved thermoelectric properties [2]. However, the electrical and thermoelectric property of the bulk crystal h-MoSi2 have not been experimentally clarified. Since t-MoSi2 is transformed into h-MoSi2 with the Ti addition by a Mechanical Alloying (MA) technique in the Mo-Ti-Si system [3], it has been reported that Mo-silicides were grown using Mo substrates and Mo-Ti alloy (Mo(Ti)) compacts by the molten salt method. However, the tetragonal phase was formed as well as the hexagonal phase in the silicides. A nonhomogeneous compositional distribution of Mo and Si atoms was observed in the silicides when using the Mo substrate and Mo(Ti) compact [4]. The single phase growth of h-MoSi2 and improved compositional homogeneity of the silicide are required.

On the other hand, MoS2 has a hexagonal structure with lattice constants of a=0.31612 and c=1.22985 nm. The detailed structure of MoS2 and extraordinary chemical properties of the two-dimensional MoS2 nanoclusters are described in Refs.5 and 6, respectively. MoS2 has a characteristic layered structure, i.e., metal chalcogenide slabs are formed by two layers of close-packed chalcogenide atoms sandwiching one metal layer between them. These slabs are stacked with only van der Waals forces between the slabs [7]. It is considered that the use of the thin separated slabs would improve the homogeneity of the atomic distribution in the resultant alloys, because the diffusing species easily can pass through the materials during the treatment. Moreover, it has also been reported that the crystalline structure of the resultant compounds is strongly affected by that of the starting materials. For example, the formation of the zincblende-MnTe phase was demonstrated using ZnTe [8]. Single phase Ca2Si was obtained using Mg2Si as the starting material [9]. In the same manner, it is expected that the h-MoSi2 would be easily obtained using MoS2 as the source material. Moreover, MoS2 has layered structures. It is expected MoSi2 synthesized by Molten salt technique by using MoS2 have nanostructures. Nanostructures have unique properties and novel applications compared to those

of bulk materials. A decrease in the thermal conductivity and an increase in the power factor, , of the nanostructures have been demonstrated by the theoretical calculations and proof of principle experiments, relative to the corresponding bulk structures.[10-13] In this study, the synthesis of h-MoSi2 was examined using MoS2 powder.

2. Experiments

The Mo-silicide powder was synthesized using MoS2 powder, S powder and a molten salt, comprised of 36.58 mol%NaCl - 36.58 mol%KCl - 21.95 mol%NaF - 4.89 mol%Na2SiF6. The salt mixture, silicon powder (99.999%, 21.85 mol% for the salt mixture), S powder [99.99 %, (5 mol% 10 mol% and 20 mol% for salt mixture] and MoS2 powder (99.9%up, 2.73 mol% for salt mixture) were placed in an SiO2–Al2O3 crucible with the powder. They were thermally treated at 773 and 873K. The structural properties of the powder were characterized by X-ray diffraction (XRD) .

3. Results and Discussion

Fig.2 Intensity ratio of MoS_2(002) and $MoSi_2$(111) by XRD spectra of the resultant powder by using S and MoS_2 as the source material at 500 ºC and 600 ºC.

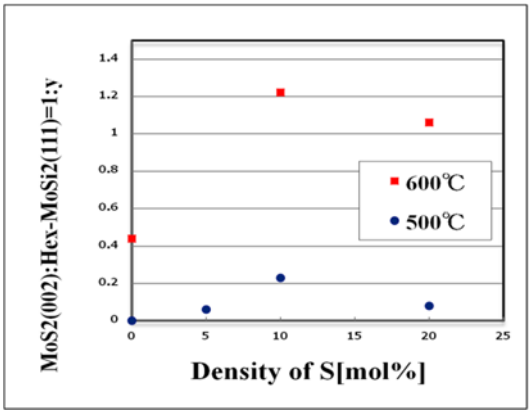

4. Conclusion

Synthesis of the h-MoSi2 was promoted by adding S atom. In case of density of S(10mol%), the effect was enhanced . It is expected that this simple growth procedure to fix the crystalline structure using the appropriate starting material.

Acknowledgements

I would like to thank D.Ishikawa and H. Tatsuoka for their fruitful discussions.

Reference

[1] APAC-SILICIDE, July 29-31, 2006, Kyoto, Thin Solid Films 515(22), pp. 8101-8300, edited by Y. Maeda, K.P. Homewood, T. Sadoh, Y. Terai, K. Yamaguchi and K. Akiyama.
[2] T. Nonomura, C. Wen, A. Kato, K. Isobe, Y. Kubota, T. Nakamura, M. Yamashita, Y. Hayakawa and H. Tatsuoka, Physics Procedia 11, 110 (2011).
[3] A. J. Heron and G. B. Schaffer, Mater. Sci. Eng. A352, 105 (2003).
[4] T. Nonomura, C. Wen, K. Shirai, K. Isobe, A. Kato, Y. Kubota, T. Nakamura, Y. Hayakawa and H. Tatsuoka, IOP Conf. Ser.: Mater. Sci. Eng. 18, 14 (2010).
[5] L. S. Byskov, J. K. Norskov, B.S. Clausen, and H. Topsoe, J. Catal. 187, 109 (1999).
[6] J. V. Lauriitsen, M. Nyberg, R.T. Vang, M.V. Bollinger, B.S. Clausen, H. Topsoe, K. W. Jacobsen, E. Laegsgaard, J. K. Norskov and F. Besenbacher, Nanotechnology 14, 385 (2003).
[7] C. F. Castro-Guerrero, F. L. Deepak, A. Ponce, J. Cruz-Reyes, M. D. Valle-Granados, S. Fuentes-Moyado, D. H. Galván and M. Jose-Yacamán, Catal. Sci. Technol. 1, 1024 (2011).
[8] T. Matsumoto, Y. Souno, H. Tatsuoka, Y. Nakanishi, H. Kuwabara, Appl. Surf. Sci. 169/170, 325 (2001).
[9] T. Hosono, M. Kuramoto, Y. Matsuzawa, Y. Momose, Y. Maeda, T. Matsuyama, H. Tatsuoka, Y. Fukuda, S. Hashimoto and H. Kuwabara, Appl. Surf. Sci. 216, 620 (2003).
[10] L. D. Hicks et al., Phys. Rev. B 47, 12727 (1993).
[11] L. D. Hicks et al., Phys. Res. B 47, 16631 (1993).
[12] R. Venkatasubramanian et al., Nature 413, 597 (2001).
[13] A. I. Hochbaum et al., Nature 451, 163 (2008)

Review on the fabrication techniques of SiGe- and Ge-on-insulator wafer

Veerappan Manimuthu[1,2], Shoma Yoshida[1,3], Yuhei Suzuki[1,4], Hiroya Ikeda[1,2,4]

1.Research Institute of Electronics, Shizuoka University
2.Graduate school of Science and technology, Shizuoka University
3.Faculty of Engineering, Shizuoka University
4.Graduate school of Engineering, Shizuoka University
*e-mail: manimuthu@rie.shizuoka.ac.jp

Abstract

The nanostructured thermoelectric materials have been expected to enhance the performance of various applications such as conversion of heat to electricity (i.e.) in the field of green energy technology, thermocooling and sensors. In order to fabricate SiGe and Ge nanowires, in this paper we survey various approaches for preparing SiGe- and Ge-on-insulator (SGOI and GOI) wafers such as SIMOX (separated by implanted oxygen) process, Ge condensation technique, direct wafer bonding process and also discusses the merits and demerits to choose better fabrication technique.

1. Introduction

Waste heat is produced on a daily basis in our life, for example laptop liberates waste heat and in the car engine, more than 70% of the energy is wasted as heat. By capturing some of these waste heat, thermoelectric materials has the ability to capture the waste heat and to charge the battery if it is placed on car. So the thermoelectric materials are the possibilities and endless.

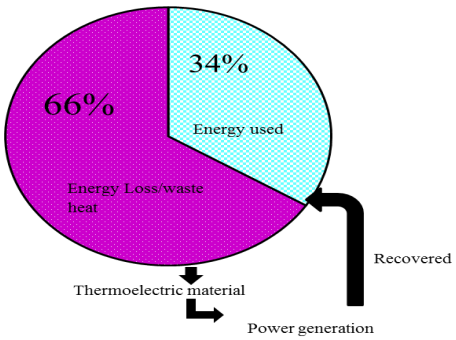

Fig. 1 Importance of thermoelectric materials.

From the Fig. 1, only 34% of total heat from different sources such as thermal power plant, nuclear power plant, automobiles, factories etc., is useful and the other 66% is still as waste heat. This energy loss or waste heat from different sources can be transferred to electrical energy by thermoelectric (materials) system. The thermoelectric effect is a phenomenon, in which the temperature difference between the hot and cold side causes the diffusion of charge carriers in the materials and thus produces electricity. Usual thermoelectric system has a pair of n- and p-type semiconductor materials (thermocouple) as shown in Fig. 2 for obtaining a large thermoelectromotive force.

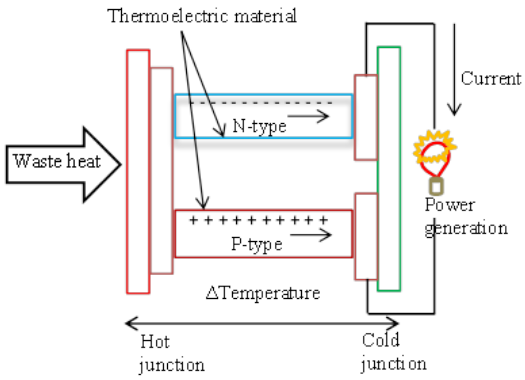

Fig. 2 Thermoelectric effect principle.

Nanostructured thermoelectric materials are expected for the enhancement of power conversion efficiency because of following factors,

1. Decrease in the thermal conductance by an increase in boundary scattering of phonons
2. Enhancement of Seebeck coefficient
3. Realization of a large number density of thermocouples by miniaturization

Another way for the improvement is usage of silicon germanium (SiGe) which has emerged as an important semiconductor technology. SiGe generally has lower thermal conductance because of an increase in defect scattering of phonons. In order to make SiGe and Ge nanowires for different thermoelectric applications this paper discusses about the different fabrication techniques for preparing SGOI and GOI wafers.

2. Fabrication processes

2.1 SIMOX process

Figure 3 shows the SIMOX process [1]. It is commonly known as separated by implanted oxygen process, which is a most popular method for Si-on insulator (SOI) fabrication. In this process there is an implantation of O ions into the Si substrate, after which ex-situ annealing at elevated temperatures removes implant damage and forms a uniform buried insulating SiO_2 layer. By optimizing fabrication conditions such as implantation substrate temperature and post-implantation annealing conditions, the crystal defects and micro-roughness of the materials can be reduced.

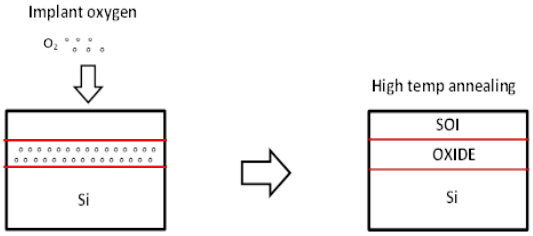

Fig. 3 Schematic diagram of SIMOX process.

The merits and demerits of SIMOX process are described below. SiGe substrates lead to acceptable buried oxide formation for low Ge concentrations, including 10% and 18% Ge. Unfortunately, when applied to higher-Ge-content SiGe, the process does not generate good quality structures for Ge concentrations greater than 30%. Surface oxidation of SiGe occurs during post-implant annealing, and thermal instability of SiGe is observed at elevated temperatures. SIMOX for SGOI and GOI fabrication has not achieved a prominent role, and other techniques have been pursued and developed.

2.2 Ge Condensation Process

This technique begins with the formation of a SiGe layer with a low Ge fraction (0.15) which was grown epitaxially by ultrahigh vacuum chemical vapor deposition over a commercially available bonded SOI wafer. Next, dry oxidation is carried out at temperatures lower than the melting temperature of SiGe in O_2 atmosphere. In this oxidation process, Si atoms in the SiGe layer are oxidized selectively and Ge atoms are rejected from the SiO_2 layers, while out-diffusion of Ge atoms is suppressed by the buried and top oxide layers, resulting in the increase of Ge fraction in the SiGe layer when the SGOI thickness becomes thinner than the initial SiGe thickness. Finally, the oxidation process is stopped when almost all Si atoms in the SGOI layer are oxidized. The schematic view of the process is shown in Fig. 4 [1, 2].

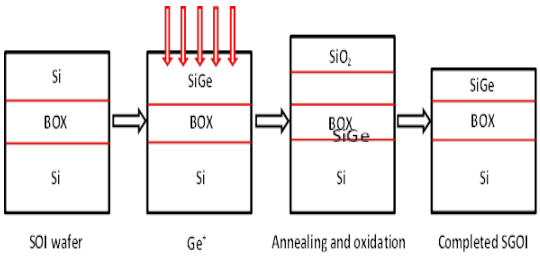

Fig. 4 Schematic diagram of Ge-condensation technique.

The merits and demerits of SIMOX process are described below. SiGe layer with very high Ge concentration can be produced. Very thin and pure layer of SGOI/GOI substrates can be produced. Growth of thick Ge layer (needed for optoelectronics) is difficult because long oxidation time is needed.

2.3 SmartCut approach

Figure 5 shows the SmartCut approach with stop layer modification [2]. The process begins with a planarized $Si_{1-x}Ge_x$ virtual substrate with the desired Ge content, followed by the growth of the stop and transfer layers at low temperatures to avoid interdiffusion. After hydrogen implantation, bonding and splitting, the created structure consists of a layer of remaining $Si_{1-x}Ge_x$ with the stop and transfer layers bonded to oxidized Si wafer. The remaining $Si_{1-x}Ge_x$ is then removed using any selective process that does not attack the stop layer, leaving behind a smooth surface. Optionally, the stop layer can then be removed leaving only the transfer layers.

The merits and demerits of SIMOX process are described below. The stop layer method has great flexibility, and can be applied to any number of transfer layers and stop layers. In addition, all layers are defined epitaxially. Thicknesses of the transferred layers are precisely controlled, allowing for the fabrication of ultrathin layers on oxide. This is ideal for fully-depleted MOSFETs.

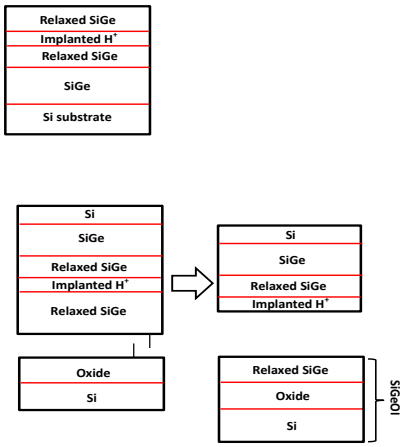

Fig. 5 Schematic diagram of SmartCut approach.

2.4 Direct wafer bonding process

In this fabrication method, at first the SiO_2 films are formed on the silicon substrates by dry oxidation. The surfaces of Ge and the oxidized Si wafer are chemically treated (ammonium hydroxide and water). The Ge and SiO_2 surfaces were then brought into contact by van der Waals attraction in a clean room at room temperature under atmospheric pressure. Ge side of the wafer is thinned by mechanical polishing. Finally, the bonded wafers are subjected to annealing for strong bonding at the interface. The schematic view of the process is shown in Fig. 6 [1, 3].

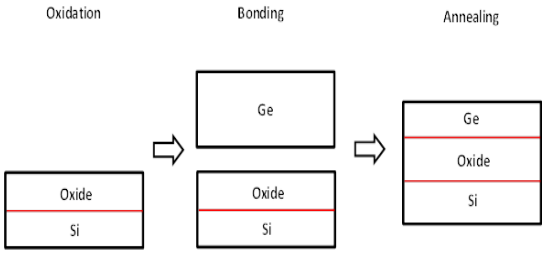

Fig. 6 Schematic diagram of direct wafer bonding process.

The merits and demerits of SIMOX process are described below. Direct wafer bonding method has the ability to create ultra-thin layers of SiGe- and Ge-on-insulator wafers. By using this process, one can control the impurity concentration and the layer thickness precisely.

3. Conclusion

On comparing the above discussed fabrication techniques, the direct wafer bonding process seems useful to study the thermoelectric characteristics of SiGe and Ge nanostructures and also for future high performance CMOS applications because of its simple procedure. Now we are confirming the bonding conditions for GOI fabrication.

References

[1] Gianni Taraschi *, Arthur J. Pitera, Eugene A. Fitzgerald, Solid-State Electronics 48 (2004) 1297–1305.

[2] Shu Nakaharai, Tsutomu Tezuka, Naoharu Sugiyama, Yoshihiko Moriyama, and Shin-ichi Takagi, Applied Physics Letters 83, 3516 (2003).

[3] Gianni Taraschi,z Arthur J. Pitera, Lisa M. McGill, Zhi-Yuan Cheng, Minjoo L. Lee, Thomas A. Langdo, and Eugene A. Fitzgerald, Journal of The Electrochemical Society, 151 (1) G47-G56 (2004).

Advantage of KFM for Seebeck Coefficient Measurement of Nanostructures

[1,2]Takuro Oda [1,3,4]Faiz Salleh [1,3,5]Hiroya Ikeda

[1]Research Institute of Electronics , Shizuoka University
[2]Faculty of Engineering , Shizuoka University
[3]Graduate School of Science and Technology, Shizuoka Uviversity
[4]Research Fellow of the Japan Society for the Promotion of Science
[5]Graduade School of Engineering , Shizuoka University

Abstract

With the aim of enhancing thermoelectric property, one of the methods is introduction of nanostructures. Therefore, a new measurement method is desired for characterizing the thermoelectric properties of nanostructured materials. In the present study, we propose a new technique of Seebeck coefficient measurement of nanostructures by KFM (Kelvin-probe force microscopy). This report demonstrates a principle of KFM and its advantage.

1. Termoelectricity and nanostructures

Thermoelectric conversion is the phenomenon to pick up heat from electricity or to pick up electricity from heat. The efficiency of thermoelectric power generation can be expressed as a function of the dimensionless figure-of-merit, ZT, which is shown in Fig 1. Z is the figure-of-merit and T is the temperature. It is found from Fig.1 that efficiency increases monotonously with increasing the ZT. Therefore, the researchers in this field have investigated to make Z large.

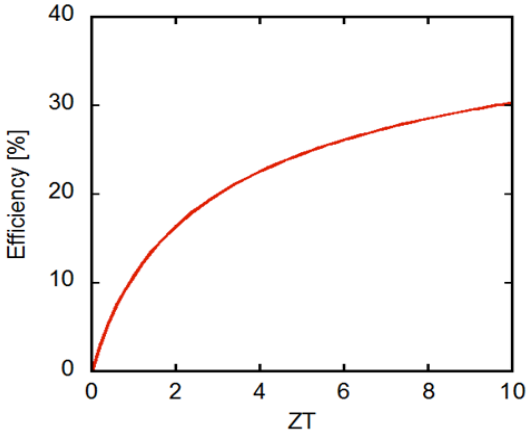

Fig. 1: Relationship between ZT and efficiency

Z is usually defind as the following equation,

$$Z = \frac{S^2\sigma}{\kappa},$$

where S is the Seebeck coefficient, σ is the electrical conductivity and κ is the thermal conductivity. Hence, the efficiency is enhanced by increasing Seebeck coefficient and by decreasing κ.

We focus our attention on silicon nanowire to increase S and to decrease κ. S is theoretically expected to increase when the diameter of silicon nanowire is smaller than 8nm [1]. This is due to the carrier confinement effect. It can be expected that when the diameter of silicon nanowire is smaller than the mean-free-path of phonon,

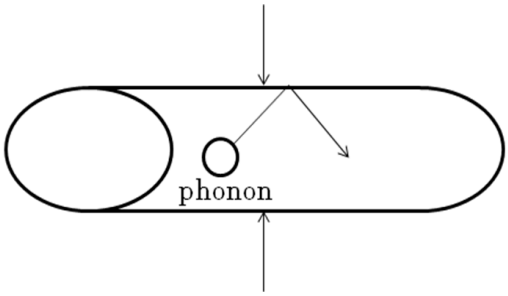

Fig. 2: Schematic diagram of boundary scattering of phonon in silicon nanowire

the value of κ decreases by increasing boundary scattering of phonon, as schematically shown in Fig.2.

2. Charactarization of nanomaterials

Unfortunately, it is difficult to measure the thermoelectric characteristics of silicon nanowire because of its small dimensions. Therefore, it is necessary to develop a new measurement method that can characteristic nanostructures. In practice, there are mainly two ways to measure the thermoelectric characteristics.

One is the fabrication of complicated sample structure by MEMS. It means that electrodes and heaters are built in the sample [3-5]. This measurement method has merits that the usual measurement devices are available and that the analysis of obtained date is simple. However, the preparation of the sample is very difficult.

The other is the usage of scanning probe microscopy [2]. A probe touches the sample surface, and thermoelectric characterization is performed in the vertical direction. Therefore, the contact between the metallic probe and the sample surface, which disturbs the thermal environment of sample, is not avoidable and specially-customized equipment is required.

We have developed a new measurement technique using KFM (Kelvin-probe force microscopy). The KFM gives us the information about the local surface potential of the sample corresponding to the Fermi-energy difference between the sample and cantilever. KFM has merits that the measurement is non-contact and easy and that special sample structure is not required.

3. Measurement principle by KFM

First of all, the measurement principle of KFM itself is explained. Fig. 3 describes the measurement principle of the Fermi energy of a sample by KFM. When a cantilever is in close proximity to the sample surface and is electrically connected to the sample, the Fermi energy of the cantilever coincides with that of the sample. Then, a Coulomb force will occur between the cantilever and the sample due to the work-function difference qΔΦ, as shown in the left side of Fig. 3. The Coulomb force is expressed as follows:

$$F = -\frac{1}{2} V^2 \frac{\partial C}{\partial z},$$

where V is the potential difference between the cantilever and the sample (or ΔΦ), C is the cantilever-sample capacitor, and z is the cantilever-sample distance.

Note that KFM nullifies this force by applying an external bias between the cantilever and the sample (V_{DC} in the right side of Fig. 3). The magnitude of this bias corresponds to the potential difference. Using the above procedure, the Fermi energy of the sample with respect to that of the cantilever can be obtained from the applied bias.

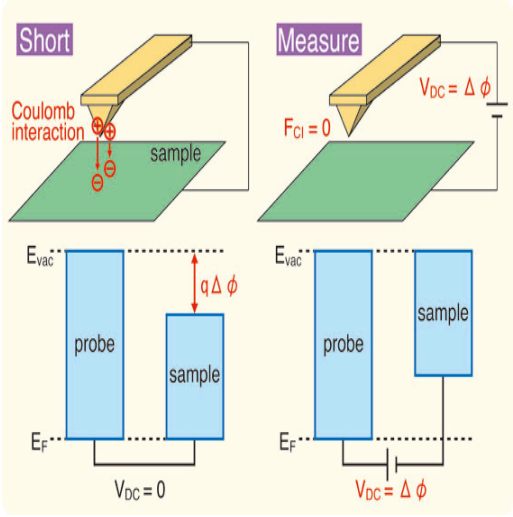

Fig. 3: The schematic view of a cantilever and the sample at the time of the KFM measurement and the corresponding band diagram

The Seebeck coefficient is defined as follows:

$$S = -\frac{\Delta V}{\Delta T},$$

where ΔV is the thermoelectromotive force, and ΔT is the temperature difference. S can be obtained by measuring the thermoelectromotiveforce for a given temperature difference across the sample. Equation of S is converted to

$$S = -\frac{\Delta V}{\Delta T} = \frac{\Phi_{TH} - \Phi_{TL}}{T_H - T_L},$$

where T_H and T_L are the temperatures in the high-temperature and low-temperature regions, respectively. Φ_{TH} and Φ_{TL} are the surface potentials in the high-temperature and low-temperature regions, respectively. Therefore, S can be estimated from the measurement of the Fermi energy for each region. Figure 4 shows the band structure of the cantilever and n-type Si sample under a temperature difference. When a temperature difference is applied to the sample, the Fermi energy of the sample will be spatially distributed. Generally, E_{FTH} is lower than E_{FTL} in n-type Si. Since KFM can measure Φ_{TH} and Φ_{TL} as shown in Fig. 4, we can evaluate the Seebeck coefficient.

4. Future plan

Now, we are preparing a Si nanowire sample and are scheduled to evaluate its Seebeck coefficient by KFM.

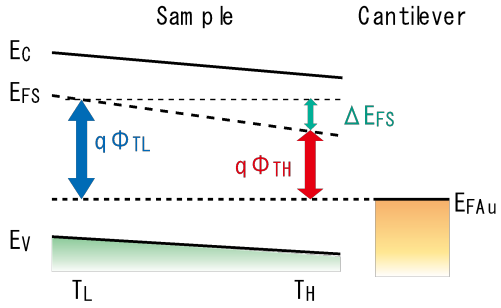

Fig. 4: Band diagram of n-type silicon and cantilever under a temperature difference

Reference

[1] N. Neophytou *et al.*, Phys. Rev. B, Vol.83, 245305 (2011)

[2] Y. Zhang, C. L. Hapenciuc, et al., Appl. Phys. Lett., vol.96, pp.62107, (2010)

[3] F. Völklein, M. Schmitt, et al., J. Electro. Mater. vol.38, pp.1109, (2009)

[4] C.-H. Lee. G. -C. Yi, et al., Appl. Phys. Lett., vol.94, pp.022106, (2009)

[5] H. J. Ryu, Z. Aksamija, et al., Phys. Rev. Lett., vol.15, pp.256601, (2010)

Fabrication of Si nanowire thermopile by focused ion beam

Yuhei Suzuki[1,2*], Faiz Salleh[1,3,4], Masaru Shimomura[2,3], Akihiro Ishida[2,3] and Hiroya Ikeda[1,2,3]

[1]Research Institute of Electronics, Shizuoka University,
Johoku 3-5-1, Naka-ku, Hamamatsu, 432-8011, Japan
[2]Graduate School of Engineering, Shizuoka University,
Johoku 3-5-1, Naka-ku, Hamamatsu, 432-8561, Japan
[3]Graduate School of Science and Technology, Shizuoka University,
Johoku 3-5-1, Naka-ku, Hamamatsu, 432-8011, Japan
[4]Fellow of the Japan Society for the Promotion of Science,
Ichibancho 8, Chiyoda-ku, Tokyo, 102-8472, Japan
TEL&FAX: +81-53-478-1335
[*]e-mail: f0330181@ipc.shizuoka.ac.jp

Abstract

With the aim of fabricating a thermopile infrared photodetector using Si nanowire thermocouples, we propose a method of alternate Ga-ion implantation by focused ion beam (FIB) into a P-doped Si-on-insulator (SOI) nanowire array. In the present study, rectangular-patterned n-type SOI layers with a P concentration of 5.1×10^{17} $cm^{-3}$was prepared, and then Ga ions were implanted into them with a dose of 4.0×10^{13} cm^{-2} and 3.5×10^{14} cm^{-2}. From the simulation of Ga ion implantation, the average Ga concentration of the Ga-implanted SOI layers was estimated to be 3×10^{18} cm^{-3} and 3×10^{19} cm^{-3}, respectively. The Seebeck coefficient of the Ga-implanted SOI layer has an opposite sign as compared with that of the original P-doped SOI layer. This result indicates that p-type Si was formed by the Ga implantation. The relationship between the average Ga concentration and Seebeck coefficient was consistent with a general characteristic of semiconductor materials.

1. Introduction

Thermoelectric semiconductors are one of the candidates for an energy harvesting since they have an ability to interconvert between thermal energy and electrical energy directly. They are usually used in the form of the thermopile that is an array of n- and p-type semiconductor connected by metal electrodes electrically in series but thermally in parallel. A thermopile infrared (IR) photodetector has been studied as an application of a thermopile [1-3]. It is composed of a thermopile equipped with an absorption film at an end. When an infrared ray is irradiated to a thermopile IR photodetector, a temperature of a thermopile on the part of an absorption film rises, and a temperature difference between the thermopile occurs. Thermopile IR photodetector observe a thermoelectromotive force corresponding to the temperature difference. The voltage sensitivity R_V of a thermopile IR photodetector is given by

$$R_V = \frac{nS\eta}{G}, \qquad (1)$$

where n is the number of thermocouples, S is the Seebeck coefficient, η is the absorption efficiency of the IR absorption film and G is the thermal conductance between the high- and low-temperature regions, which is proportional to the thermal conductivity. It is obvious from eq. (1) that a high-sensitive thermopile IR photodetector requires a thermopile material with a high Seebeck coefficient and a low thermal conductivity.

Thermoelectric properties of semiconductor materials depend on its impurity concentration. With increase in the impurity concentration, the Seebeck coefficient decreases and the thermal conductivity increases. The Fermi level should be controlled for high R_V because Fermi level of semiconductor determines its impurity concentration. In parallel, it is needed to enhance thermoelectric parameters themselves.

Introduction of nanowire thermopile to infrared photodetector is expected to enhance R_V through an increase in the number of thermocouples by miniaturization, an increase in the Seebeck coefficient by a carrier confinement effect [4,5], and a decrease in the thermal conductivity by increase in the rate of the boundary scattering of phonons [6,7]. These are why we have investigated thermoelectric characteristics of nanostructured Si [8-15]. Therefore, the construction of process techniques for a Si nanowire thermopile is essential for practical device fabrication. We propose a method for preparing a nanowire thermopile in a Si-on-insulator (SOI) wafer as shown in Fig. 1. First of all, the array of n-type Si nanowires is patterned in an n-type SOI wafer, in which one end of the wires is connected by an n-type Si pad. Then, Ga ions are alternately implanted into the n-type Si nanowires by focused ion beam (FIB) to form p-type Si nanowires. FIB enables us to precisely control the implantation to Si nanowires with high reproducibility because it has high spatial resolution and fine adjustment of the dose of implanted ions. Finally, the n- and p-type nanowires are electrically connected by depositing an Al electrode on the Si pad.

In the present study, in order to make sure the forming p-type Si by FIB implantation, we performed the implantation of Ga ions by FIB into P-doped n-type Si wires. Then, the Seebeck coefficient was measured for the original P-doped Si and the Ga-implanted Si.

2. FIB conditions based on Ga implantation simulation

The depth profile of implanted Ga ion within the SOI layer was simulated to determine the FIB implantation conditions such as the dose of Ga ions and the acceleration voltage of Ga ions. Since crystalline defects are produced in the SOI layer during the ion implantation process, the SOI wafer has to be annealed after the Ga implantation for recovering the crystallinity. Hence, the distribution of thermally-diffused Ga ions by post-annealing was also taken into account.

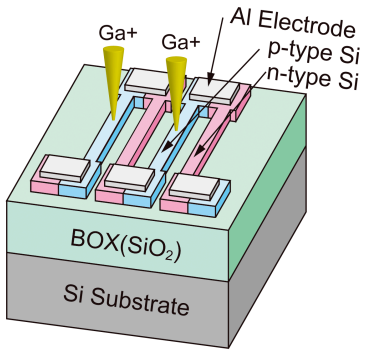

Fig. 1 Fabrication procedure of a Si nanowire thermopile by using FIB Ga ion implantation.

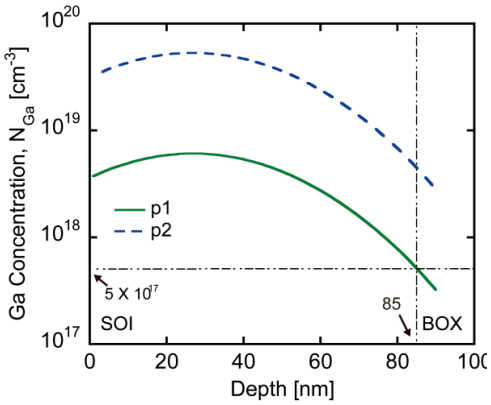

Fig. 2 Ga concentration profile in the SOI layer after annealing.

The simulation of implanting Ga ion accelerated through 30 kV into the SOI layer with a thickness of 85 nm was performed for a dose of 4.0×10^{13} cm^{-2} and 3.5×10^{14} cm^{-2}. Then, the thermal diffusion of Ga ions by the annealing at 830 ^{o}C for 20 minutes was calculated. The final Ga concentration profile in the SOI layer is shown in Fig. 2. The original P concentration N_P, which was determined to be 5.1×10^{17} cm^{-3}, is also shown in the figure. Because it is found from Fig. 2 that the Ga concentration is larger than the P concentration at the whole position of the SOI layer, it is predicted that p-type SOI layers are formed without p-n junctions for these implantation conditions. In addition, the average Ga concentration in SOI layers was estimated from the Ga concentration profile, which is 3×10^{18} cm^{-3} and 3×10^{19} cm^{-3}, respectively. The dose of Ga ion and the average Ga concentration N_{Ga} in the SOI layer used in this study are summarized in Table 1.

Table 1 P concentration N_P, Ga dose and average Ga concentration N_{Ga} for SOI samples prepared in this study. Measured Seebeck coefficients are also listed.

	N_P [cm^{-3}]	Dose [cm^{-2}]	N_{Ga} [cm^{-3}]	S [mV/K]
n-type	5.1×10^{17}	-	-	-0.357
p1	5.1×10^{17}	4.0×10^{13}	3×10^{18}	0.331
P2	5.1×10^{17}	3.5×10^{14}	3×10^{19}	0.245

3. Sample preparation and measurement procedure

SOI wafer with the area of 1 × 1 cm^2 was cut, and the thickness of SOI layer was 340 nm. SOI layer was thinned to a thickness of 85 nm by repeating thermal oxidation and HF etching, and then P atoms were thermally doped into the SOI layer at 830 °C for 20 minutes. The P concentration in the SOI layer was estimated to be 5.1×10^{17} cm^{-3} from four-probe resistance measurement at room temperature. A number of n-type Si wires with a width of 500 nm and a length of 1 mm were patterned by SiO_2 mask, electron beam lithography and KOH etching. Si pads with an area of 1.2 × 0.5 mm^2 were also patterned at the both ends of Si wires for TEMF measurement. Ga ions were implanted according to the FIB conditions determined in Sec. 2 with the implantation angle of 7 ° for avoiding a channeling effect [16]. Al electrodes with an area of 0.4 × 0.4 mm^2 were deposited on the Si pads. The thickness of buried oxide layer was 400 nm and the p-type Si substrate had an impurity concentration of 10^{15} cm^{-3}.

Seebeck coefficient was measured using the same method as that used in our previous investigations [8,9,13]. The measurement setup is depicted in Fig. 3. The two gilded Cu plates were arranged with a gap of 1 mm. The SOI sample was bridged on the gap. A resistive heater was attached to one of a pair of Cu plates. Therefore, by heating one side of the sample, the temperature difference between both ends of the wire was produced, and the TEMF corresponding to the temperature difference was generated. The time evolutions of the TEMF and the temperature of the SOI surface at the low temperature side T_L and the high temperature side T_H were simultaneously measured. From these data, we can obtain the Seebeck coefficient as a function of average temperature.

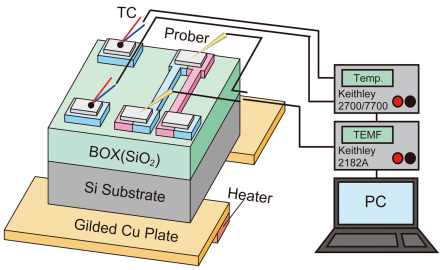

Fig. 3 Schematic diagram of Seebeck coefficient measurement system.

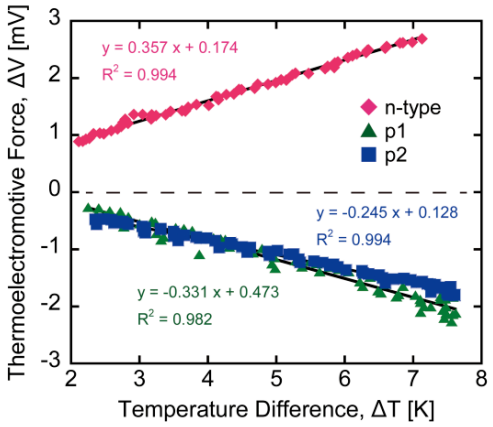

Fig. 4 Measured TEMF of original P-doped and Ga-implanted SOI layers as a function of temperature difference.

During the TEMF and temperature measurement, the Seebeck coefficient was almost constant in an average temperature range from 340 K to 380 K. Therefore, the average Seebeck coefficient S was evaluated from the gradient of relationship between the TEMF ΔV and the temperature difference $\Delta T = T_H - T_L$ as given by $S = -\Delta V/\Delta T$.

4. Result and discussion

Figure 4 shows the TEMF ΔV measured as a function of temperature difference ΔT for the original n-type and implanted SOI samples. It is clearly found that the TEMF of

the implanted SOIs shows negative values while the n-type SOI has positive TEMF. This sign inversion indicates that p-type Si was successfully formed by the Ga implantation. The relationship between the TEMF and the temperature difference can be fitted by a straight line, which evidences that the SOI layer has a constant Seebeck coefficient in the measurement temperature range. The Seebeck coefficients for original P-doped and Ga implanted SOI layer are listed in Table 1. The Seebeck coefficient of the p2 sample with a larger dose is found to be smaller than that of the p1 sample. In general, absolute value of Seebeck coefficient in semiconductor materials decreases with increase in its carrier concentration [17-19]. Hence, the relationship between the measured Seebeck coefficients of implanted SOI layers and the dose amount is consistent with the general property, and we can control the Seebeck coefficient of p-type Si nanowire through the dose of implanted Ga ions.

5. Conclusion

We proposed and investigated a method of alternately implanting Ga ion by FIB into the array of P-doped Si wires for fabricating a Si nanowire thermopile. The measured TEMF of Ga-implanted SOI layer shows an opposite sign as compared with the TEMF of original P-doped SOI layer. From this result, it is found that the SOI layer changed from n-type to p-type by Ga implantation into P-doped SOI layer. The measured Seebeck coefficient of highly Ga-implanted SOI layer was smaller than that of SOI layer with a lower dose. This result is consistent with the tendency of characteristics in general semiconductor materials. Consequently, Ga-ion implantation by FIB can be applied to fabrication of a Si nanowire thermopile.

Acknowledgment

This work was financially supported by a Grant-in-Aid for Challenging Exploratory Research (No. 24651168) and a Grant-in-Aid for JSPS Fellows (No. 23·6002) from the JSPS.

Reference

[1] M. Hirota, Y. Nakajima, M. Saito, F. Satou and M. Uchiyama, Proc. SPIE **5359** (2004) 111
[2] J. Schieferdecker, R. Quad, E. Holzenkämpfer and M. Schulze, Sensors and Actuators A: Phys. **46** (1995) 422
[3] M. Müller, W. Budde, R. Gottfried-Gottfried, A. Hübel, R. Jähne and H. Kück Sensors and Actuators A: Phys. **54** (1996) 601
[4] L. D. Hicks and M. S. Dresselhaus, Phys. Rev. B **47** (1993) 16631
[5] N. Neophytou and H. Kosina, J. Electron, Mater. **41** (2012) 1305
[6] A. I. Hochbaum, R. Chen, R. D. Delgado, W. Liang, E. C. Garnett, M. Najarian, A. Majumdar and P. Yang, Nature **451** (2008) 163.
[7] A. I. Boukai, Y. Bunimovich, J. Tahir-Kheli, J. K. Yu, W. A. Goddard III and J. R. Heath, Nature **451** (2008) 168
[8] F. Salleh, K. Asai, A. Ishida and H. Ikeda, Appl. Phys. Express **2** (2009) 071203
[9] F. Salleh, K. Asai, A. Ishida and H. Ikeda, J. Autom. Mobile Rob. & Intell. Syst. **3** (2009) 134
[10] H. Ikeda and F. Salleh, Appl. Phys. Lett. **96** (2010) 012106
[11] F. Salleh and H. Ikeda, J. Electron. Mater. **40** (2011) 903
[12] F. Salleh and H. Ikeda, Adv. Mater. Res. **222** (2011) 197
[13] F. Salleh, K. Miwa and H. Ikeda, J. Adv. Res. Phys. **3** (2012) 021207
[14] F. Salleh, Y. Suzuki, K. Miwa and H. Ikeda, Proc. The 13th Int. Conf. on QiR (Quality in Research) (IEEE Xplore) (2013) 931
[15] F. Salleh, Y. Suzuki, K. Miwa and H. Ikeda, Appl. Phys. Lett. **103** (2013) 062107
[16] S. M. Sze, Semiconductor Devices Physics and Technology, Sec. 10.4.3, Wiley, 1985
[17] T. H. Geballe and G. W. Hull, Phys. Rev. **98** (1955) 940
[18] G. D. Mahan, Solid State Phys. **51** (1997) 81
[19] O. Yamashita and N. Sadatomi, Jpn. J. Appl. Phys. **38** (1999) 6394

New Measurement Method of Thermal Conductivity for Si Nanowire

[1,2]Shoma Yoshida, [1,3]Yuhei Suzuki, [1,4]Veerappan Manimuth,
[3,4] Masaru Simomura, [3,4]Kenji Murakami, [1,3,4] Hiroya Ikeya,

[1]Research Institute of Electronics, Shizuoka University
[2]Faculty of Engineering, Shizuoka University
[3]Graduate School of Engineering, Shizuoka University
[4]Graduate School of Science and Technology, Shizuoka University

Abstract

This paper introduces a new measurement method of heat transport characteristics for Si nanowire. In this method, we can measure the thermal diffusivity without touching and destroying the sample. Therefore we can expect diversification of measurement environment as well as easy measurement procedure and high throughput.

1. Background

Thermoelectric materials can interconvert between heat and electric power and have some benefits which are no movable parts, maintenance free, miniaturization and environment-friendly energy conversion. However there are some problems for practical use. They are insufficient efficiency and low thermoelectromotive force. Therefore, we want to enhance efficiency of thermoelectric conversion.

Figure 1 shows relationship between the power generation efficiency and ZT. The figure-of-merit Z is expressed as

$$Z = S^2\sigma / \kappa \qquad (1)$$

where S is the seebeck coefficient, σ is the electric conductivity and κ is the thermal conductivity. From Fig. 1, we have to increase Z to enhance the efficiency. Equation 1 shows Z is inversely proportional to thermal conductivity. Therefore, one of the enhancement of the efficiency is reduction of thermal conductivity. Heat transport phenomenon is conducted by lattice vibration. From the point of view of quantum mechanics, it is regarded as the particle called for phonon. Phonon mean free path is average distance between phonon scatterings. Specifically, λ_{ph} is the parameter characterizing phonon scatterings. Thermal conductivity decreases when the diameter of wire is smaller than phonon mean free path. Figure 2 shows the comparison between two wires with large and small diameter. λ_{ph} is the phonon mean free path. If nanowire diameter is smaller than λ_{ph}, the probability of phonon collision at nanowire wall increases.

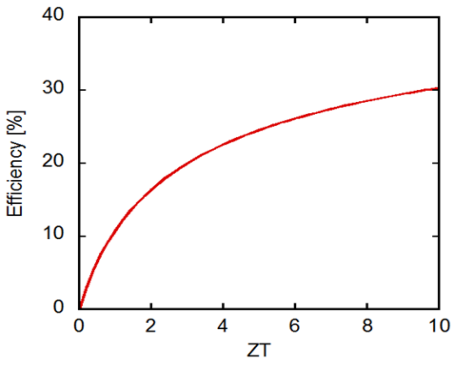

Fig.1 Relationship between the power generation efficiency and ZT

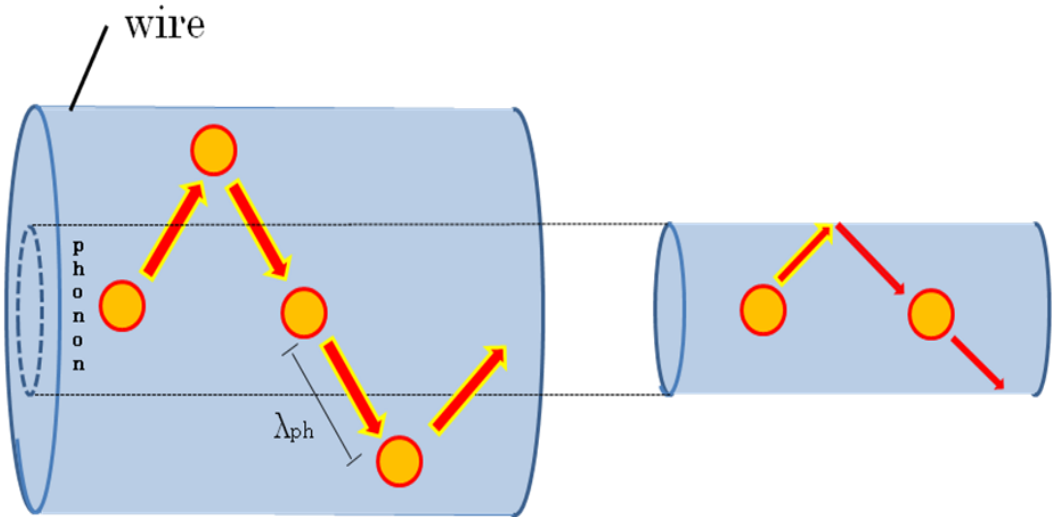

Fig. 2 Relationship between the wire diameter and phonon mean free path

Therefore, phonon momentum or velocity gets lower. This leads to the decrease in thermal conductivity.

For this purpose, we use nanostructured materials such as nanowire.

2. Measurement Method

Measurement of thermal conductivity for nanowires is very difficult. We have an idea about a new method based on the principle of AC calorimetry method to measure thermal diffusivity [1]. Figure 3 is a schematic diagram of AC calorimetry. Laser is irradiated to the surface of sample to provide heat flux and measure the time delivering heat to thermocouple (TC). Then, we measure the change of heat travelling time(δt) with changing L. Finally, we evaluate thermal diffusivity from the relationship between L and δt.

First of all, we are constructing a measurement system of thermal diffusivity for bulk materials as shown in Fig. 4. In this system, we put an oscillation signal into halogen lamp from function generator, by which the sample is periodically heated. The heat propagates through the sample and we detect temperature by pyrometer. At that time, we observe the delay time of AC temperature by lock-in amplifier with respect to the reference AC source.

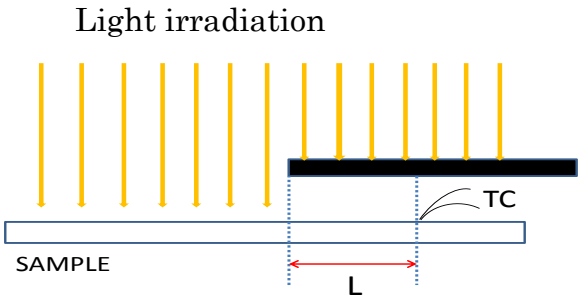

Fig. 3 Schematic diagram of AC calorimetry method.

3. Future Plan

Now, we are constructing the system on measurement using a lock-in amplifier for detecting δt and its analysis procedure. In the next step, we will observe the thermal diffusivity of Si wafer and SiO_2 layer as a reference.

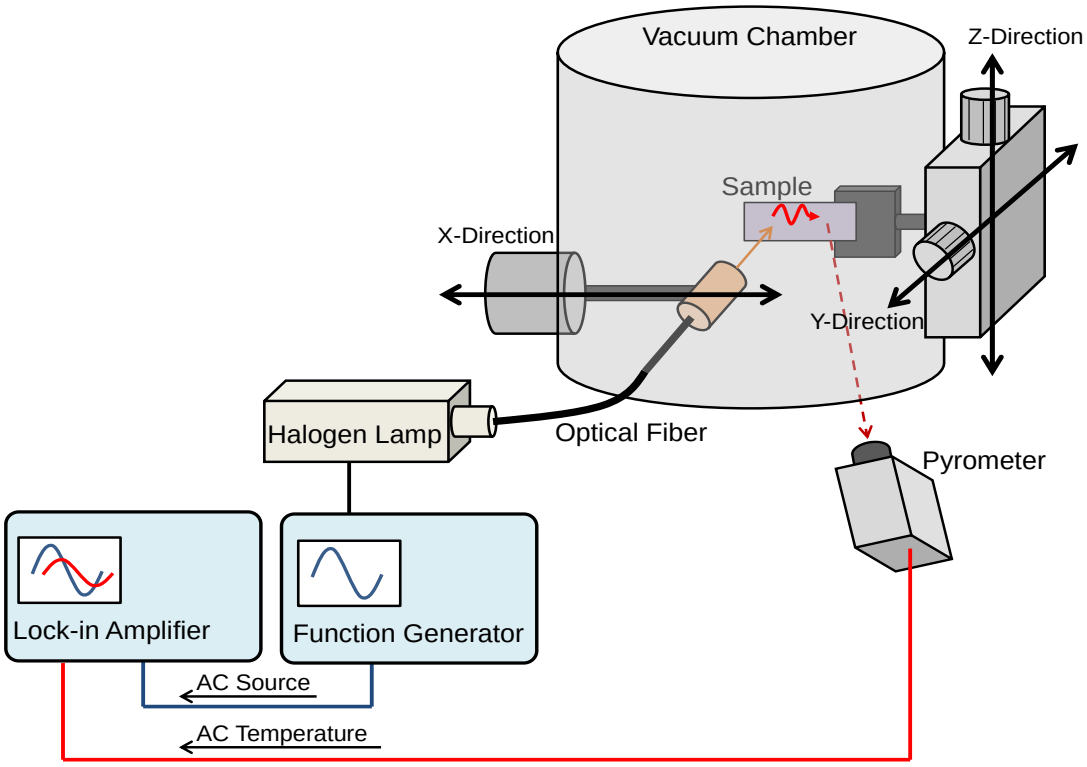

Fig. 4 Schematic diagram of measurement system

Reference

[1]I. Hatta, Y. Sasuga, R. Kato and A. Maezono, Rev. Sci. Instrum. 56 (1985) 1643

Improvement of DSSC through surface modification

Rangga Winantyo[1] and Kenji Murakami[2]
[1]Graduate School of Science and Technology, Shizuoka University, Japan
[2]Graduate School of Engineering, Shizuoka University, Japan

Abstract

One dimensional nano-wire ZnO has been studied to enhance electrical properties of Dye Sensitized Solar Cells. Different ZnO nano-structures were synthesized by using different ZnO salts through water bath deposition. After calcination, nano-structures on FTO surface were observed. The nano-structure profile was evaluated to see the effect on cell's electrical properties. Better aligned nano-structure was formed by using zinc acetate as precursor solution.

1. Introduction

DSSC is one potential candidate for next-generation solar cells, because it does not require a material with high purity so that the cost of the production process is relatively low.

DSSC's performance can be improved by decreasing the electron-hole recombination rate and by increasing the light-harvesting capability. ZnO is a semiconductor material with a band gap around 3.37 eV at room temperature, which is similar to TiO_2 (3.2eV)[1]. In the present study, we are investigating the method to enhance the cell's performance through surface modification.

2. Experimental

a. Preparation of ZnO thin film

The ZnO thin films were deposited on the FTO coated glass substrate by using hydrothermal method. All the substrates were cleaned with ethanol and acetone using ultrasonic cleaner. The ZnO nanostructured thin film was grown through hydrothermal method by immersing the substrate in a mixture of 5 mM zinc acetate $(CH_3COO)_2Zn.2H_2O$, zinc nitrate hexahydrate $Zn(NO_3)_2$ and 5 mM hexamethylene tetramine $(CH_2)_6N_4$ at 90^0C for 2 hours.

b. DSC preparation

Platinum (Pt) coated glass was used as a counter electrode. The ZnO thin film was dipped into Ruthenium dye (N719) solution

for 24 hours. The DMPII electrolyte was used in this experiment.

c. Characterization method

Bunkoh Keiki-JASCO solar simulator was used to measure the solar cell efficiency. The measurement was done under 1.5AM.

3. Result and Discussion

From the measurement result in Fig.1, it can be seen that the efficiency is slightly increased.

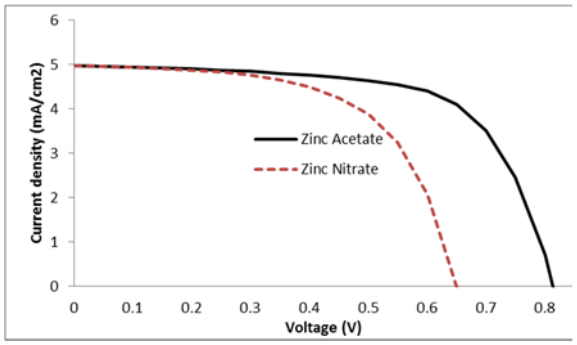

Fig.1 I-V measurement of ZnO DSC based on zinc acetate and based on zinc nitrate.

By using the zinc acetate to grow vertically aligned nanowire, the efficiency of the cell raises from 1.9% to 2.4%. From Fig.2, we also can see that there are changes in the morphology of the nanostructure.

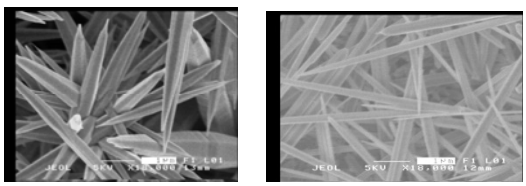

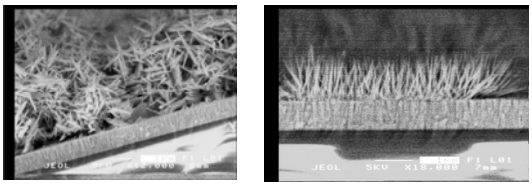

Fig.2 Nanostructure of DSC based on zinc nitrate (left) and zinc acetate(right).

4. Conclusion

A well-aligned ZnO nanowire array was synthesized for improving the cell's efficiency. Our preliminary conclusion suggests that the efficiency can be increased by changing the form of the nanostructure.

References

[1] Phattalung, Sutassana, Na., Smith, Michael, F., and Limpijumnong, Sukit, "First Principles Study of NativeDefects in Anatase TiO_2," Suranaree University of Technology (SUT), 2006

Crystal Structures of K_2PtCl_6 and related materials

Yuya Shirahashi

Graduate School of Engineering, Shizuoka University,
3-5-1 Johoku, Naka-ku, Hamamatsu 432-8561, Japan
*e-mail: f0330175@ipc.shizuoka.ac.jp

Abstract

Crystal structure of K2PtCl6 and related materials were analyzed. They are having a crystal structure similar, but they have different characteristics. The structural properties of the resultant composites were characterized by X-ray diffraction (XRD).

1. Introduction

Platinum and its compounds has been widely used because platinum has characteristics of chemically very stable and hardly-oxidized. For example, platinum has been applied to fuel cell and electrode, and medical, catalyst purification of exhaust gas of automobile because of platinum has the high melting point and catalytic activities, anti-microbial activities. [1]

However, the structure of the platinum compounds isn't known in many cases. Therefore, knowing the structure of the platinum compound is important in order to expand the range of applications.

This paper shows growth mechanism and detailed structure of K_2PtCl_6 and related materials.

2. Experiments

Platinum compounds has been synthesized as a source material K_2PtCl_6 and H_2PtCl_6. First, Platinum compounds were synthesized by source material, CsCl and I/KI. Second, platinum compounds were obtained by drying the solution. The structural properties of the compounds were characterized by X-ray diffraction (XRD).

3. Results and Discussion

Figure1 shows XRD spectra of the resultant powder by using H_2PtCl_6 as the source material. Figure1 shows that the compounds consist of Cs_2PtI_6. This compounds consists of a single-phase Cs_2PtI_6.

Figure2 shows XRD spectra of the resultant powder by using K_2PtCl_6 as the source material. Figure2 shows that the compounds consists of three materials. The peak of K_2PtCl_6 is caused by residual source material because K_2PtCl_6 is not soluble. The peak of Cs_2PtI_6 appeared by the synthesis of K_2PtCl_6 and Cs, I_2. The peak of Cs_2PtCl_6 appeared as an intermediate product because reaction was not sufficient. The amount of the resulting compounds is more in the order of K_2PtCl_6, Cs_2PtI_6, and Cs_2PtCl_6 from the peak intensity. The Peak appears in the order of Cs_2PtI_6, Cs_2PtCl_6 and K_2PtCl_6 in the same Miller indices from the difference in lattice constant.

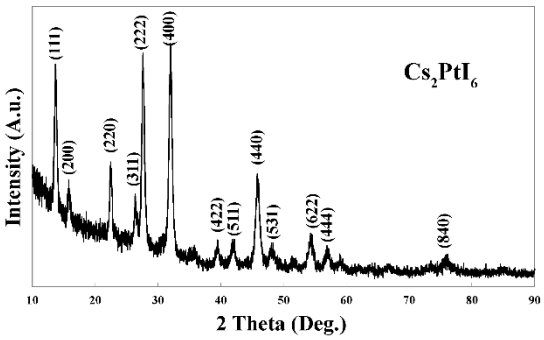

Figure1. XRD spectra of the resultant powder by using H_2PtCl_6 as the source

material.

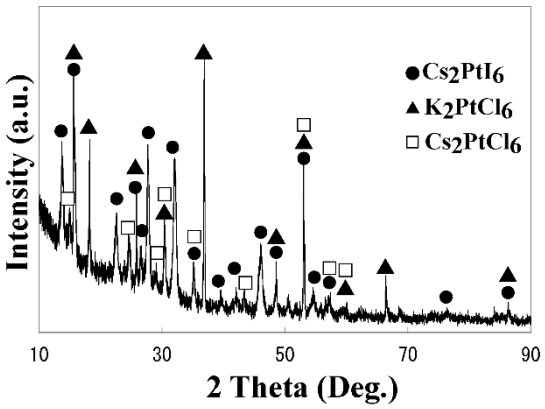

Figure2. XRD spectra of the resultant powder by using H_2PtCl_6 as the source material.

4. Conclusion

Cs_2PtI_6 was synthesized by source material (K_2PtCl_6 or H_2PtCl_6) and CsCl, I_2/KI. As a results, the crystal structure of K_2PtCl_6 and related materials can be estimated.

In future, the crystal structure of another related materials of K_2PtCl_6 will be analyzed.

5. Reference

[1]Kyung-Hwan Cho, Jong-Eun Park, Tetsuya Osaka, Soo-Gil Park, Volume 51, Issue 5, 10 November 2005, Pages 956–960